The thermal impedance integral and the pathway decomposition of supercritical turbulent heat transfer. Part II. Experimental validation and scope of the linearised pathway form

Ivan Otić*

Institute for Thermal Energy Technology and Safety
Karlsruhe Institute of Technology
Eggenstein-Leopoldshafen, Germany

Özgür Ertunç

Fluid Dynamics and Spray Laboratory
Mechanical Engineering, Özyeğin University
İstanbul, Türkiye

Abstract

In Part I the generalised Lyon integral was shown to become a thermal impedance when the pseudocritical barrier sweeps the boundary layer, and a two-point quadrature at the barrier yielded the linearised pathway form LinP, $\mathrm{Nu}_b = \sqrt{\mathrm{Re}_b}\,\mathrm{Pr}_b^{-1/2}(\mathrm{Pr}_b/\mathrm{Pr}_w)^{1/4}$, with the symmetric weight $w = 1/2$ and $\beta = 1/2$ fixed from classical correlation families. LinP is tested here in two stages against an experimental database spanning supercritical water at 23.5–24.5 MPa and CO_2 at 9 MPa, Reynolds numbers 2.5×10^4 to 2×10^6, Prandtl numbers 0.8 to 14, and upward, downward and horizontal pipes. The first stage operates directly on the measured impedance. Across 2201 measurement stations the wall-to-bulk impedance bias falls from 76 % for Dittus–Boelter to 6 % for the pathway form, and the effective pathway weight crosses 1/2 at the bulk pseudocritical crossing for both fluids and all Reynolds numbers, a parameter-free confirmation of the symmetric weight. The second stage tests LinP predictively in the engineering-relevant Q-mode against the bulk-anchored entangled Bishop and the wall-anchored entangled Swenson correlations and the uncorrected Dittus–Boelter. The penetration scaling $\mathrm{Nu} \sim \sqrt{\mathrm{Re}}$ is preferred over $\mathrm{Re}^{0.8}$ wherever the barrier is active. Uncalibrated and density-uncorrected, LinP carries the lowest case-mean root-mean-square wall-temperature error, 31.5 K against 47.9, 54.3 and 55.1 K. Its residual deficits, confined to the deterioration peaks and the downflow regimes, trace to one missing ingredient: the pathway-resolved density correction beyond the linearised form.

Keywords: supercritical water; supercritical CO2; heat transfer deterioration; wall temperature; Nusselt correlation; forced convection

*Corresponding author: ivan.otic@kit.edu

Nomenclature

Roman symbols

C	correlation prefactor [–]
c_p	isobaric specific heat [$\mathrm{J\,kg^{-1}\,K^{-1}}$]
$\bar{c}_p$	integrated mean specific heat, $(h_w - h_b)/(T_w - T_b)$ [$\mathrm{J\,kg^{-1}\,K^{-1}}$]
d	pipe inner diameter [m]
f	Darcy friction factor [–]
$\mathcal{F}$	bracket function of the pathway form [–]
G	mass flux [$\mathrm{kg\,m^{-2}\,s^{-1}}$]
Gr	Grashof number, $g\,\lvert\rho_b - \rho_w\rvert\,\rho_b\,d^3/\mu_b^2$ [–]
h	specific enthalpy [$\mathrm{J\,kg^{-1}}$]
L	heated length [m]
Nu	Nusselt number [–]
Pr	Prandtl number [–]
$\overline{\mathrm{Pr}}$	modified Prandtl number, $\bar{c}_p\mu/\lambda$ [–]
q_w	wall heat flux [$\mathrm{W\,m^{-2}}$]
Re	Reynolds number [–]
Ri	Richardson number, $\mathrm{Gr}/\mathrm{Re}_b^2$ [–]
T	temperature [K]
T_{pc}	pseudocritical temperature [K]
w	pathway weight [–]; w_{eff} effective pathway weight
x	axial coordinate [m]
Z	thermal impedance, $(T_w - T_b)/q_w$ [$\mathrm{K\,m^2\,W^{-1}}$]

Greek symbols

α	heat transfer coefficient [$\mathrm{W\,m^{-2}\,K^{-1}}$]
β	resistance exponent of the pathway conductance [–]
θ_{pc}	barrier position, $(T_{pc} - T_b)/(T_w - T_b)$ [–]
λ	thermal conductivity [$\mathrm{W\,m^{-1}\,K^{-1}}$]
μ	dynamic viscosity [Pa s]
ξ	logarithmic Prandtl ratio, $\ln(\mathrm{Pr}_b/\mathrm{Pr}_w)$ [–]
ρ	density [$\mathrm{kg\,m^{-3}}$]

Subscripts

b, w	bulk, wall
pc	pseudocritical
exp	experimental
in, out	pipe inlet, outlet

Abbreviations

DB	Dittus–Boelter correlation
DBs	uncalibrated Dittus–Boelter diagnostic, $\mathrm{Re}_b^{0.8}\mathrm{Pr}_b^{0.4}$
LinP	linearised pathway form
HTD	heat transfer deterioration
TFD	thermally fully developed
Q-mode, T-mode	prediction from heat flux / from measured wall temperature
IQR	interquartile range
RMS	root-mean-square
NTUU	National Technical University of Ukraine dataset
GK	Grabezhnaya–Kirillov dataset
JIHT RAS	Joint Institute for High Temperatures of the Russian Academy of Sciences dataset

1 Introduction

1.1 Background: the impedance integral and the linearised pathway form

The companion paper ([1], see §1) derives a generalised Lyon integral from the Favre-averaged energy equation for variable-property turbulent pipe flow and shows that the constant-property Lyon integral, a thermal resistance, becomes a thermal impedance when properties vary strongly between wall and bulk. The impedance character is carried by three features: capacitive thermal storage at the c_p peak, history dependence through the axially sweeping pseudocritical barrier, and response lag in the perpetually developing thermal profile. Each of the three classical property-ratio correction factors is traced to a distinct component of the framework: the Prandtl ratio $(\mathrm{Pr}_b/\mathrm{Pr}_w)^p$ and the density ratio $(\rho_w/\rho_b)^r$ to the molecular and turbulent parts of the impedance integrand, and the integrated specific heat ratio $(\bar{c}_p/c_{p,b})^q$ to the enthalpy-to-temperature conversion outside the integral. Ten classical correlations are shown to map onto a single general structure (55) (Part I) differing only in the choice of reference temperature, exponent values, and degree of entanglement between the factors.

We recall from Part I ([1]) that the general form combining the three classical correction factors is

$$\mathrm{Nu}_b = C\,\mathrm{Re}_b^n\,\mathrm{Pr}_b^m \left(\frac{\mathrm{Pr}_b}{\mathrm{Pr}_w}\right)^p \left(\frac{\bar{c}_p}{c_{p,b}}\right)^q \left(\frac{\rho_w}{\rho_b}\right)^r, \tag{1}$$

in which the Prandtl and density ratios enter through the impedance integrand and the integrated specific-heat ratio through the conversion pre-factor. The exponent p encodes the fractional importance of the pseudocritical barrier ($p \to 0$ when the barrier dominates, $p \to 2/3$ when the sublayer does); q is eliminable; r captures the density-driven modification of the turbulent bypass factor.

The pseudocritical barrier is identified as the source of the impedance character: when the barrier lies within the boundary layer it sweeps radially as the bulk temperature rises, continuously resetting the thermal profile and violating the fully developed equilibrium that underpins the classical $\mathrm{Re}/\ln\mathrm{Re}$ scaling [2]. The resulting penetration-depth scaling is $\mathrm{Nu} \sim \sqrt{\mathrm{Re}}$ in the barrier-dominated regime. A two-point pathway quadrature of the impedance integral at the pseudocritical isotherm, combined with this scaling, yields the linearised pathway form

$$\mathrm{Nu}_b = C\sqrt{\mathrm{Re}_b}\,\mathrm{Pr}_b^{-\beta}\left(\frac{\mathrm{Pr}_b}{\mathrm{Pr}_w}\right)^{w\beta}, \tag{2}$$

with $C = 1$ adopted uncalibrated (C of order unity by construction), the symmetric pathway weight $w = 1/2$, the unique unbiased assignment of the two-point quadrature, and the resistance exponent $\beta = 1/2$ fixed a priori from the Mikheev–Žukauskas correlation family. No modified Prandtl number, no $\bar{c}_p/c_{p,b}$ factor, and no fitted parameter are introduced. The integrated specific heat ratio is eliminated as an artefact of enthalpy-to-temperature conversion. The entanglement of this artefact with the physical Prandtl correction through the modified Prandtl number $\overline{\mathrm{Pr}}_b = \bar{c}_p\,\mu_b/\lambda_b$ is identified as a source of spurious behaviour near the pseudocritical temperature in Part I ([1]). The calibrated Dittus–Boelter prefactor 0.023 is shown analytically to be entangled with the $\mathrm{Re}^{0.8}$ exponent through the Prandtl–von Kármán friction law [2], and an uncalibrated form $\mathrm{Nu}_b = \mathrm{Re}_b^{0.8}\mathrm{Pr}_b^{0.4}$ (denoted DBs) is introduced as a diagnostic for this entanglement.

1.2 Scope of the validation

The four structural problems of the Nusselt-correlation framework identified in [1], §1.1 – the Q-mode circularity of wall-evaluated properties, the spatial mismatch of the wall and bulk trajectories through the pseudocritical region, the fragmentation of the literature into more than two hundred correlations fitted to particular fluids and property tables, and the inadequacy of the fully developed $\mathrm{Re}^{0.8}$ scaling under the strong axial property variation that the pseudocritical region produces – furnish the structural tests that the validation must confront. The present paper tests the three predictions of the scaling analysis in the predictive Q-mode against an experimental database spanning supercritical water at 23.5–24.5 MPa ([3, 4]; Grabezhnaya and Kirillov [5]; Yamagata et al. [6]) and CO_2 at 9 MPa ([7, 8]), with Reynolds numbers from 2.5×10^4 to 2×10^6, Prandtl numbers from 0.8 to 14, and upward, downward, and horizontal pipe configurations. An eighteen-case subset with significant pseudocritical crossings is selected for the case-by-case predictive comparison; diagnostic analysis uses the full database of 2201 measurement stations.

Three established correlations serve as comparators, arranged along the entanglement axis of the general form (1): [9], bulk-anchored with the entangled $\overline{\mathrm{Pr}}_b$ and a density ratio $(\rho_w/\rho_b)^{0.43}$; [10], wall-anchored with the entangled $\overline{\mathrm{Pr}}_w$ and a density ratio $(\rho_w/\rho_b)^{0.231}$; and Dittus–Boelter, the uncorrected baseline. LinP occupies the symmetric interior point between the two one-sided entangled limits and carries no density correction. The comparison is therefore diagnostic: whether the symmetric, disentangled, uncalibrated, density-uncorrected LinP resolves the structural pathology that each one-sided entangled correlation must reproduce when the pseudocritical barrier sweeps through the boundary layer.

1.3 Structure of the paper

Section 2 reports the diagnostic analysis: the departure of the experimental property fields from the thermally fully developed assumption, the experimental bracket function $\mathcal{F}_{\mathrm{exp}}$ and its comparison against the parallel-pathway envelope, the effective pathway weight $w_{\mathrm{eff}}(\theta_{pc})$ and its crossing through $w = 1/2$ at the bulk pseudocritical point, and the impedance-ratio comparison between Dittus–Boelter and LinP. Section 3 reports the predictive Q-mode validation: the numerical setup, the eighteen-case subset, and a case-by-case reading of the wall-temperature profiles organised by the Reynolds-exponent test (§3.5), the disentangled Prandtl-correction test (§3.6), and a structural summary of the validation (§3.7). Section 4 consolidates the results and identifies the open problems.

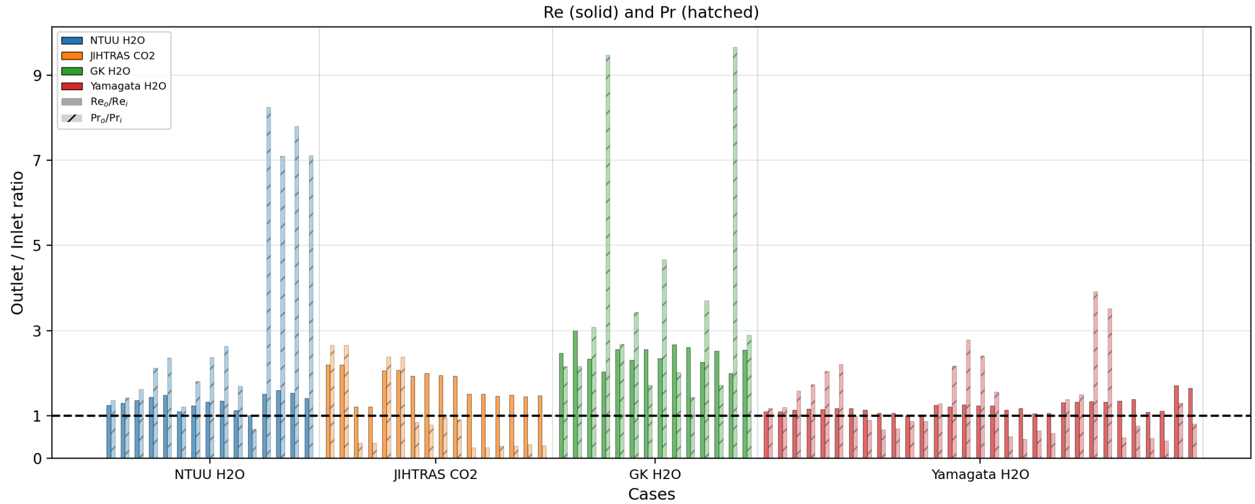

Figure 1: Outlet-to-inlet property ratios per case. Solid bars: $\mathrm{Re}_b(x_{\mathrm{out}})/\mathrm{Re}_b(x_{\mathrm{in}})$; hatched bars: $\mathrm{Pr}_b(x_{\mathrm{out}})/\mathrm{Pr}_b(x_{\mathrm{in}})$. Dashed line marks the TFD condition.

2 Departure from thermal equilibrium

The analysis of Sections 6.1.3 and 6.1.4 (Part I) predicts that the thermally fully developed (TFD) assumption is violated whenever the pseudocritical barrier is active. We now test this quantitatively using 2201 measurement locations drawn from four experimental datasets spanning two distinct property landscapes: water at 23.5–24.5 MPa ([3, 4] (15 regimes: 13 upflow, 2 downflow; in the following referred to as NTUU), Grabezhnaya and Kirillov [5] (14 regimes, all upflow; in the following referred to as GK), [6] (31 regimes, all horizontal; each condition measured at the bottom and at the top wall, recorded as separate regimes; in the following referred to as Yamagata)) and CO_2 at 9 MPa ([7, 8] (16 regimes: 10 upflow, 6 downflow; in the following referred to as JIHTRAS, after the Joint Institute for High Temperatures of the Russian Academy of Sciences)). The database thus provides upflow, downflow, and horizontal flow configurations. Throughout, case labels such as #555 refer to the case numbering of the database. All cases satisfy $\mathrm{Ri} = \mathrm{Gr}/\mathrm{Re}_b^2 < 0.105$, where the Grashof number is evaluated per measurement station in the density-difference form $\mathrm{Gr} = g\,|\rho_b - \rho_w|\,\rho_b\,d^3/\mu_b^2$, so the database is treated as forced convection throughout , see e.g. Çengel and Ghajar [11]. The threshold is consistent with the mixed-convection criteria surveyed by Jackson [12]. Jackson's buoyancy parameter Bo^* provides an alternative onset criterion; the residual orientation sensitivity of the matched upflow/downflow pairs below the Ri threshold is examined in §3.6.

Property variation along the pipe. In TFD constant-property flow, Re_b, Pr_b, and λ_b are invariant along the pipe axis. Figure 1 shows the outlet-to-inlet ratios of Re_b and Pr_b for every case in the database. The departures are severe and not perturbative corrections – properties change up to an order of magnitude along the heated length.

Figure 2 plots the coefficient of variation $\mathrm{CoV}(Z_{\mathrm{exp}}) = \sigma(Z)/\mu(Z)$ of the experimental impedance $Z_{\mathrm{exp}}(x) = \frac{T_w(x)-T_b(x)}{q_w}$, against q_w/G, where $\sigma(Z)$ and $\mu(Z)$ denote the standard deviation and the mean of Z_{exp}, respectively. The impedance variation does not scale monotonically with q_w/G across fluids, reflecting the distinct thermodynamic properties of H_2O and CO_2 and the influence of flow orientation.

In the following, the binned median trend is commonly evaluated. It is constructed by sorting

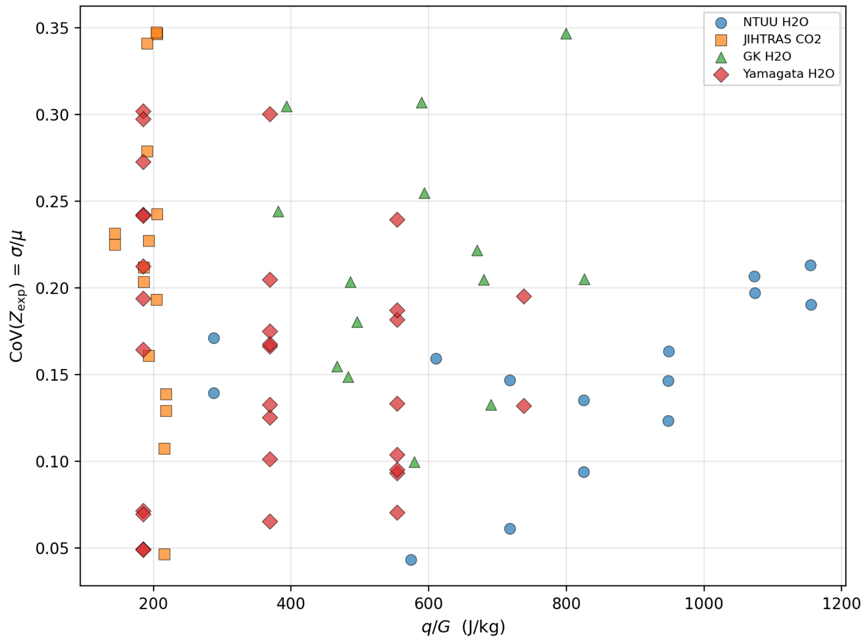

Figure 2: Coefficient of variation of the experimental thermal impedance $Z_{\rm exp}$ versus q_w/G.

the data points by the control variable and dividing them into up to 15 equal-count bins (each containing ≥ 15 points). The curve represents the median response as a function of the median control variable per bin, with shading indicating the interquartile range (25–75 percentile) (IQR).

Impedance structure at the pseudocritical crossing. Figure 3 displays the experimental thermal impedance $Z_{\rm exp}$ versus θ_{pc} with a binned median per fluid. The lower-Re_b datasets (NTUU, GK, Yamagata) exhibit a sudden change in the binned median near $\theta_{pc} \approx 0$. The JIHTRAS CO_2 data show a rapid sequence of local extrema reflecting the fact that all bulk-evaluated properties (Re_b, Pr_b, ρ_b, λ_b) undergo their steepest transition when T_b passes through T_{pc}. The fast oscillating crossover is consistent with their narrower θ_{pc} range. The oscillation is the impedance signature of a smooth but rapid property crossover, not a thermodynamic singularity.

The bracket function and its bounds. The parallel pathway Nusselt number (75) (Part I) factorises, with $\xi = \ln(\mathrm{Pr}_b/\mathrm{Pr}_w)$, as

$$\mathrm{Nu}_b = C\sqrt{\mathrm{Re}_b}\,\mathrm{Pr}_b^{-\beta}\;\underbrace{\big[w\,e^{\beta\xi} + (1-w)\big]}_{\mathcal{F}_{\rm parallel}(\xi)}, \tag{3}$$

in which the bracket function carries the entire wall-side Prandtl dependence. For small ξ the bracket expands as

$$\mathcal{F} = 1 + w\beta\,\xi + \frac{w\beta^2}{2}\,\xi^2 + \cdots \tag{4}$$

and LinP (84) (Part I) follows by exponentiating the first-order term: $\mathcal{F}_{\rm LinP} = e^{w\beta\xi} = (\mathrm{Pr}_b/\mathrm{Pr}_w)^{w\beta}$.

In general, we write $\mathrm{Nu}_b = C\sqrt{\mathrm{Re}_b}\,\mathrm{Pr}_b^{-1/2} \times \mathcal{F}(\xi,\,\theta_{pc},\,\ldots)$, where $\xi = \ln(\mathrm{Pr}_b/\mathrm{Pr}_w)$, $C = 1$, and where the bracket function $\mathcal{F}$ contains the wall-side Prandtl dependence. The first factor requires only bulk quantities determined by the energy balance; $\mathcal{F}$ is where the nonlinearity of the impedance integral lies.

The experimental bracket function is evaluated as $\mathcal{F}_{\rm exp} = \mathrm{Nu}_b^{\rm exp}\,/\,(\sqrt{\mathrm{Re}_b}\,\mathrm{Pr}_b^{-1/2})$ for the entire forced-convection database.

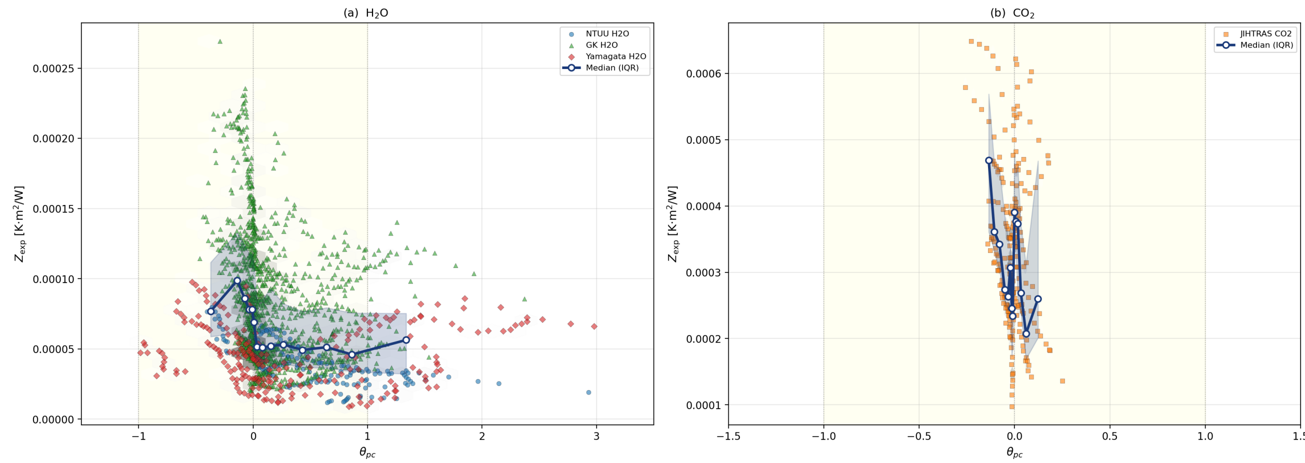

Figure 3: Experimental thermal impedance Z_{exp} versus barrier position θ_{pc}, separated by fluid. Scatter coloured by dataset with binned median with IQR shading per dataset. The yellow shaded region marks the effective barrier $\theta_{pc} \in [-1, 1]$. The oscillatory structure near $\theta_{pc} = 0$ reflects the bulk-property crossover at $T_b = T_{pc}$.

Within the two-pathway framework, i.e., if the Nusselt number is assumed to depend on the wall-side properties only through $\xi = \ln(\mathrm{Pr}_b/\mathrm{Pr}_w)$ with w, $\beta = 1/2$ fixed and no further enhancement mechanism, the parallel pathway (3) is limited. The limits are, therefore, indicative bounds: any density-driven bypass modification, θ_{pc}-dependent prefactor, or a steeper effective β inside the barrier can push $\mathcal{F}_{\text{exp}}$ above the parallel envelope.

Figure 4 plots $\mathcal{F}_{\text{exp}}$ against ξ. Panel (a) colours each station by θ_{pc}. At $\xi = 0$ ($\mathrm{Pr}_w = \mathrm{Pr}_b$, constant properties), the data pass through $\mathcal{F} \approx 1$, as required. For moderate property contrast ($|\xi| \lesssim 0.5$), the scatter is centred on the parallel and LinP envelopes ($\mathcal{F}_{\text{LinP}} = \mathrm{e}^{\xi/4}$), particularly confirming that the first-order expansion captures the leading behaviour. For $\xi \gtrsim 0.5$ ($\mathrm{Pr}_b \gg \mathrm{Pr}_w$), the data spread upward and, for a substantial fraction of the results, above the parallel envelope, organised systematically by θ_{pc}: locations inside the effective barrier ($|\theta_{pc}| \leq 1$) tend toward the highest $\mathcal{F}_{\text{exp}}$, while locations outside the barrier remain closer to LinP.

The envelope being exceeded at high ξ indicates that dependence on the wall-side $\mathrm{Pr}_b/\mathrm{Pr}_w$ alone with w, $\beta = 1/2$ fixed cannot reproduce the barrier enhancement. An additional factor, such as θ_{pc}-dependence in w (or the prefactor) or the density-ratio correction ρ_w/ρ_b, is needed.

Panel (b) shows the binned median of $\mathcal{F}_{\text{exp}}$ over all data, with the inter-quartile range (IQR) shaded. The vertical shaded band marks the inter-quartile range of ξ for locations classified as lying outside the effective barrier, i.e. with $|\theta_{pc}| > 1$ so that the pseudocritical peak sits outside the bulk–wall temperature interval. For those locations $\mathrm{Pr}_b \approx \mathrm{Pr}_w$, so $\xi \approx 0$ and $\mathcal{F} \approx 1$; the band shows where the central 50% of such locations actually fall along the ξ-axis. The range $\xi \gtrsim 0.5$ marks the barrier-dominated regime, beyond which $\mathrm{Pr}_b/\mathrm{Pr}_w$ is large enough that the peak of the pseudocritical property impedes turbulent transport across the boundary layer. It is an empirical boundary, where the binned median leaves the pathway envelope. In this regime, the binned median rises monotonically from $\mathcal{F} \approx 1.2$ at $\xi = 0.5$ to $\mathcal{F} \approx 2.1$–2.4 at $\xi \approx 2.3$. The binned median therefore is located above the parallel envelope across the whole barrier-dominated range, by $\sim$5–20%, confirming that the two-pathway-Pr-only framework is not rich enough to bracket the data: the excess is the physical signature of the additional θ_{pc} and/or density-ratio dependence noted above. The departure $\Delta\mathcal{F} = \mathcal{F}_{\text{exp}} - \mathcal{F}_{\text{LinP}}$ is structured rather than stochastic, confirming that the

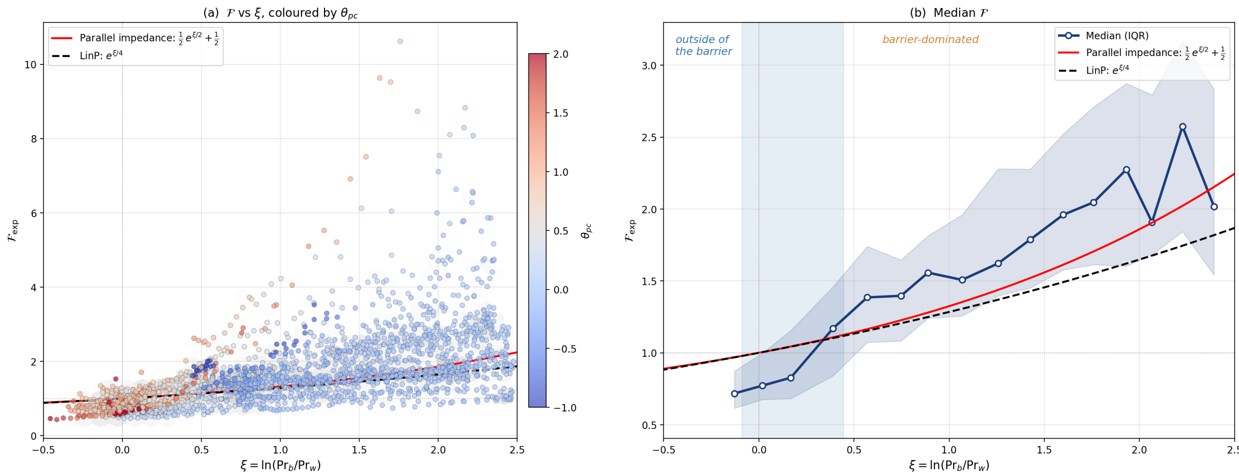

Figure 4: Bracket function $\mathcal{F}_{\text{exp}}$ versus $\xi = \ln(\mathrm{Pr}_b/\mathrm{Pr}_w)$. (a) Scatter coloured by barrier position θ_{pc}; curves show the parallel (upper) and LinP (lower) envelopes. (b) Median with inter-quartile (IQR) shading, with the same parallel and LinP references. The vertical shaded band shows the inter-quartile range of the barrier-influenced regime for all ξ with $|\theta_{pc}| > 1$ (outside of the barrier).

higher-order nonlinearity of the impedance integral is amenable to systematic parametrisation.

The effective pathway weight w_{eff}. Inverting the parallel bracket (3) for w at fixed $\beta = 1/2$ isolates the pathway weight from the experimental data. Writing $\mathcal{F}_{\text{parallel}} - 1 = w\,(e^{\beta\xi} - 1)$ and substituting the measured bracket, the effective pathway weight is defined as

$$w_{\text{eff}} = \frac{\mathcal{F}_{\text{exp}} - 1}{e^{\beta\xi} - 1} \tag{5}$$

and evaluated per station. The extraction is ill-conditioned as $\xi \to 0$ (both the numerator and the denominator vanish), so the analysis is restricted to $|\xi| = |\ln(\mathrm{Pr}_b/\mathrm{Pr}_w)| > 0.1$, which retains the barrier-entry and barrier-dominated locations where the property contrast is resolvable.

Figure 5 shows w_{eff} as a function of θ_{pc} across all datasets. At the pseudocritical bulk crossing ($\theta_{pc} \approx 0$), the binned median passes through $w_{\text{eff}} \approx 0.5$ for both fluids: for CO_2 (JIHTRAS, $\mathrm{Re_b}$ up to $\sim 2 \times 10^6$) the two bins straddling $\theta_{pc} = 0$ give $w_{\text{eff}} = 0.47$ and 0.52; for H_2O (NTUU, GK, Yamagata) the central bins give $w_{\text{eff}} \approx 0.40$–$0.60$. The crossing value $w_{\text{eff}}(\theta_{pc} \approx 0) \approx 1/2$ is invariant under Reynolds number, working fluid, and pressure. For high-Reynolds-number JIHTRAS cases, the values oscillate tightly about the mean, whereas the lower-Reynolds-number water data exhibit greater scatter. The value $w = 1/2$ adopted in the LinP (2) is therefore consistent with the empirical w_{eff} at the crossing. Apart from the crossing, $w_{\text{eff}}(\theta_{pc})$ departs from 1/2 in a structured manner: the binned medians rise for $\theta_{pc} > 1/2$. The values of w_{eff} that exceed unity indicate that the two-pathway model with w and β fixed cannot account for the full barrier enhancement. The excess is the same effect that carries $\mathcal{F}_{\text{exp}}$ above the parallel envelope in Figure 4. This θ_{pc}-dependence is the mechanism by which the linearised form underestimates the impedance in the barrier-dominated regime: the model is anchored at the crossing ($w_{\text{eff}} \approx 1/2$) but does not represent the drift of w_{eff} as the barrier sweeps through the boundary layer. A parametrisation of $w(\theta_{pc})$, or equivalently a density-ratio correction correlated with θ_{pc}, is therefore the natural next step; the result $w_{\text{eff}}(\theta_{pc} \approx 0) \approx 1/2$ provides the anchoring condition.

Impedance ratio: Dittus–Boelter versus LinP. The thermal impedance $Z = (T_w - T_b)/q_w$ and the ratio $Z_{\text{exp}}/Z_{\text{model}}$ measure how far the experimental heat transfer departs from a given

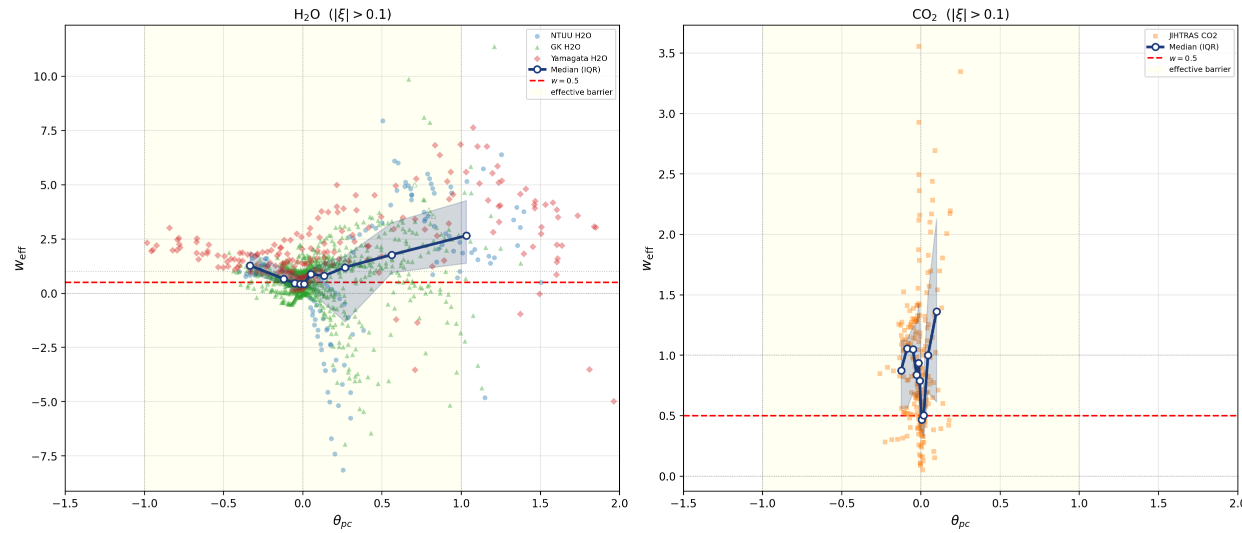

Figure 5: Effective pathway weight $w_{\text{eff}}(\theta_{pc})$ versus barrier position θ_{pc}, evaluated for locations with $|\xi| = |\ln(\mathrm{Pr}_b/\mathrm{Pr}_w)| > 0.1$ (outside this band the definition (5) is ill-conditioned). Symbols: experimental data; solid line: binned median shaded with IQR; dashed line: $w = 1/2$. Both binned medians cross $w_{\text{eff}} \approx 1/2$ at $\theta_{pc} \approx 0$.

correlation. Figure 6 compares the Dittus–Boelter and LinP predictions as functions of barrier position θ_{pc}.

The DB ratio (Figure 6(a)) exhibits a sharp, nearly symmetric spike at $\theta_{pc} = 0$, where T_b passes through T_{pc} and all bulk properties undergo their steepest variation. Outside the effective barrier ($|\theta_{pc}| > 1$), the ratio relaxes toward unity. As a consequence of the constant-property Lyon integral, the DB correlation precisely isolates the effects of the Prandtl number variation in the vicinity of $\theta_{pc} = 0$ (Figures 6a and 1a (Part I)). Because Z_{exp} is the thermal impedance, the median of $Z_{\text{exp}}/Z_{\text{DB}}$ (Figure 6a) recovers the mirrored Pr profile (Figure 1a (Part I)).

By contrast, the LinP ratio (Figure 6b) shows a structured but significantly smaller crossover: the binned median rises smoothly to unity as $\theta_{pc} \to 0^-$, exhibiting a small jump at $\theta_{pc} \approx 0$, to approach unity again for $\theta_{pc} > 0$. The correction $\mathrm{Pr}_b/\mathrm{Pr}_w$ resolves the leading-order sublayer impedance, and the residual structure is organised rather than stochastic. However, LinP induces dispersion for $\theta_{pc} > 0$, indicating the need for the additional θ_{pc} and density-ratio corrections noted above.

Table 1 quantifies the comparison across four scaling choices. LinP achieves the lowest overall bias (median ratio 0.94), while pure $\sqrt{\mathrm{Re}_b}$ without the Prandtl correction is 27% high and the full Dittus–Boelter is 76% high. The $\mathrm{Pr}_b^{-1/2}\,(\mathrm{Pr}_b/\mathrm{Pr}_w)^{1/4}$ correction thus reduces the median impedance error from 76% to 6%.

The diagnostic chain establishes four results. First, TFD is violated by orders of magnitude: properties change by factors of 2–10 along the heated length.

Second, the barrier position θ_{pc} organises the impedance residual; the $\mathrm{Pr}_b/\mathrm{Pr}_w$ correction reduces the median bias from 76% to 6%.

Third, the bracket function clusters near the LinP prediction for the moderate property ratio but departs systematically, rather than stochastically, for large $\mathrm{Pr}_b/\mathrm{Pr}_w$. It exceeds the parallel envelope in the barrier-dominated regime ($\xi \gtrsim 0.5$), indicating that the two-pathway Pr-only framework requires an additional θ_{pc} or density-ratio dependence.

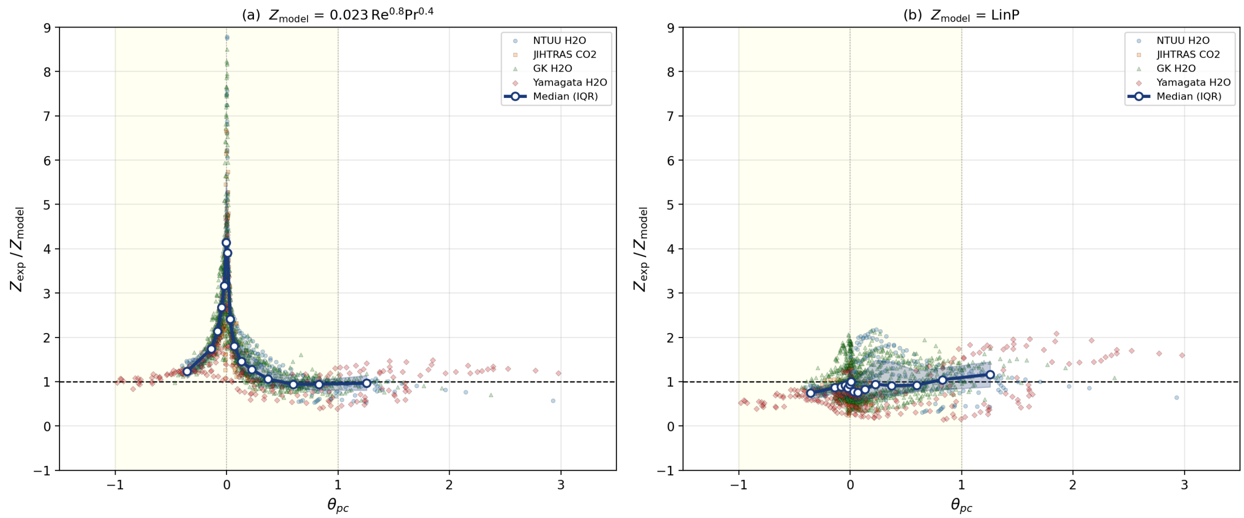

Figure 6: Impedance ratio $Z_{\text{exp}}/Z_{\text{model}}$ versus barrier position θ_{pc}. (a) Dittus–Boelter ($\text{Nu}_b = 0.023\,\text{Re}_b^{0.8}\,\text{Pr}_b^{0.4}$). (b) LinP ($\text{Nu}_b = \sqrt{\text{Re}_b}\,\text{Pr}_b^{-1/2}\,(\text{Pr}_b/\text{Pr}_w)^{1/4}$). Solid line: binned median; shaded band: interquartile range. Yellow shading marks the effective barrier $\theta_{pc} \in [-1,\, 1]$.

Dataset	$\text{Re}^{1/2}$	LinP	$0.023\,\text{Re}^{0.8}$	DB
NTUU H_2O	1.29	1.12	1.13	1.33
JIHTRAS CO_2	1.02	0.78	1.52	2.60
GK H_2O	1.67	1.20	1.32	2.28
Yamagata H_2O	1.00	0.78	0.86	1.18
All (median)	1.27	0.94	1.20	1.76

Table 1: Impedance ratio $Z_{\text{exp}}/Z_{\text{model}}$ by scaling choice and dataset; the per-dataset rows are means, the final row is the median over all 2201 stations. "$\text{Re}^{1/2}$": $\text{Nu}_b = \sqrt{\text{Re}_b}$ (no Prandtl term); "LinP": full linearised pathway (2); "$0.023\,\text{Re}^{0.8}$": DB prefactor and exponent without $\text{Pr}_b^{0.4}$; "DB": full Dittus–Boelter.

Fourth, the $\theta_{pc} = 0$ crossover is a wall-to-bulk-property event whose impedance signature is oscillatory rather than singular.

These findings quantify the structural limitation identified in Section 6.1.3 (Part I): the Lyon integral determines Nu_b from the full wall-to-bulk temperature profile, a functional dependence that no finite set of property ratios can encode. The bracket function $\mathcal{F}(\xi,\, \theta_{pc})$ quantifies the shape of this missing information but does not resolve it.

LinP captures the leading-order correction and yields bounded, physically consistent predictions.

In the following, we assess the predictive performance of LinP in the Q-mode – the engineering scenario of primary interest, in which the wall temperature T_w is unknown and must be obtained iteratively (see also Part I). The Q-mode predictions are compared against experimental wall temperature profiles and benchmarked against the DB, Bishop, and Swenson correlations.

3 Numerical implementation and validation

3.1 Computational framework

The solver ("VarTherm") discretises the pipe into N axial segments and iterates in enthalpy rather than temperature, eliminating errors that arise when the temperature-based energy balance is used near T_{pc} where c_p may vary by an order of magnitude within a single segment. At each segment:

1. Fluid properties (ρ, μ, c_p, λ, h) at the local (P, T_b) are obtained from CoolProp library, [13].

2. T_w is determined iteratively with under-relaxation ($\omega = 0.7$) until the relative change falls below 10^{-4}.

3. The friction factor is computed from the explicit Haaland equation, [14]:

$$f = \left\{ -1.8 \, \log_{10} \left[\left(\frac{\varepsilon/d}{3.7} \right)^{1.11} + \frac{6.9}{\mathrm{Re}} \right] \right\}^{-2}. \tag{6}$$

4. The increase in enthalpy per segment is $\Delta h = q_w \, \pi \, d \, \Delta x / \dot{m}$, and T_b is recovered from the equation of state. Pressure is updated via the Darcy–Weisbach relation.

The pseudocritical temperature T_{pc} at local pressure is determined by maximising $c_p(T)$ over a bracketing interval. All thermophysical properties are computed locally as temperature and pressure dependent quantities using the CoolProp library [13].

3.2 Experimental database and numerical setup

The database used for validation comprises experimental cases across four datasets spanning two fluids: supercritical water at 23.5–24.5 MPa ([3, 4] (NTUU); Grabezhnaya and Kirillov [5] (GK); [6]) and CO_2 at 9 MPa ([7, 8] (JIHTRAS)).

The eighteen-case subset presented below comprises the regimes in which the wall or the bulk crosses the pseudocritical temperature within the heated length, together with the matched upflow/downflow pairs and pre-crossing entries of the same datasets, which serve as moderate-variation controls; the subset includes the strongest heat transfer deterioration (HTD) cases of the database. mass fluxes from 506 to 2193 kg/(m^2 s), heat fluxes from 236 to 2534 kW/m^2, pipe diameters from 6.25 to 22.7 mm, and reduced pressures P/P_c from 1.065 to 1.22. Tables 2–6 summarise the conditions for each dataset. Cases include upflow, downflow and horizontal flow cases. In all cases, the stainless steel pipe walls are hydraulically smooth.

Parameter	**Case 1** (#555)	**Case 2** (#565)	**Case 3** (#574)	**Case 4** (#583)
Fluid	Water			
Pipe inner diameter d	6.25 mm			
Heated length L (mm)	600	600	480	360
Pressure P (MPa)	23.5 ($P/P_c = 1.065$)			
Mass flux G ($\mathrm{kg/(m^2\,s)}$)	2193	2193	2193	2193
Wall heat flux q_w ($\mathrm{kW/m^2}$)	1810	2080	2355	2534
q_w/G (J/kg)	825	948	1074	1155
T_{in} (K)	642.7	643.1	643.3	642.7
T_{pc} (K)	≈ 652.6			

Table 2: Experimental conditions for the four supercritical water test cases (NTUU database, vertical tube, upward flow). All cases enter near T_{pc}.

Parameter	**Case 5** (#104)	**Case 6** (#145)
Fluid	Water	
Pipe inner diameter d (mm)	6.25	9.50
Heated length L (mm)	600	600
Pressure P (MPa)	23.5 ($P/P_c = 1.065$)	
Mass flux G ($\mathrm{kg/(m^2\,s)}$)	509	248
Wall heat flux q_w ($\mathrm{kW/m^2}$)	802	510
q_w/G (J/kg)	1576	2056
T_{in} (K)	640.2	573.2
T_{pc} (K)	≈ 652.6	

Table 3: Experimental conditions for the two supercritical water downflow test cases (NTUU database, vertical tube, downward flow).

Parameter	**Case 1** (#42)	**Case 2** (#43)	**Case 3** (#44)	**Case 4** (#45)
Fluid	CO_2			
Pipe inner diameter d	22.7 mm			
Heated length L	2950 mm			
Pressure P (MPa)	9.0 ($P/P_c = 1.22$)			
Mass flux G ($\mathrm{kg/(m^2\,s)}$)	2100	2100	2140	2140
Wall heat flux q_w ($\mathrm{kW/m^2}$)	428	428	413	413
q_w/G (J/kg)	204	204	193	193
T_{in} (K)	307.9	307.9	307.6	307.6
T_{pc} (K)	≈ 313.2			

Table 4: Experimental conditions for the four supercritical CO_2 test cases (JIHTRAS database, vertical tube, upward and downward flow).

Parameter	**Case 1** (#53)	**Case 2** (#54)	**Case 3** (#58)	**Case 4** (#62)
Fluid	Water			
Pipe inner diameter d	10 mm			
Heated length L	4000 mm			
Pressure P (MPa)	$\sim$24			
Mass flux G (kg/(m^2 s))	987	1491	1002	506
Wall heat flux q_w (kW/m^2)	789	739	681	236
q_w/G (J/kg)	799	496	680	466
T_{in} (K)	591.9	625.8	623.7	625.2
T_{pc} (K)	≈ 654 (at $P \approx 24$ MPa)			

Table 5: Experimental conditions for the four supercritical water test cases (Grabezhnaya and Kirillov [5] (GK), upward vertical tube).

Parameter	**Case 1** (#111)	**Case 2** (#112)	**Case 3** (#121)	**Case 4** (#122)
Fluid	Water			
Pipe inner diameter d	7.5 mm			
Heated length L	1500 mm			
Pressure P (MPa)	24.5			
Mass flux G (kg/(m^2 s))	1260	1260	1260	1260
Wall heat flux q_w (kW/m^2)	698	698	930	930
q_w/G (J/kg)	554	554	738	738
T_{in} (K)	574	578	651	652
T_{pc} (K)	≈ 656.2			

Table 6: Experimental conditions for the four supercritical water test cases (Yamagata et al. [6], horizontal tube). Cases #111/#121 are bottom-wall and #112/#122 top-wall records of the same two runs.

Axial resolution and iteration tolerance are $N = 1000$ and 10^{-4}, respectively; convergence was verified by halving the tolerance and reducing the segment count to 800, both of which left the predicted $T_w(x)$ unchanged to the plotting precision. All results presented below use the resolution $N = 1000$ and tolerance 10^{-4}.

The VarTherm bulk temperature predictions are in excellent agreement with all datasets that provide bulk temperature measurements ([3], [6]); the comparison therefore isolates the Nusselt correlation rather than the energy balance.

3.3 Models tested

Four Nusselt correlations are compared in Q-mode (heat flux specified, wall temperature predicted iteratively). All share the Haaland friction factor (Eq. 6).

1. **DB** ([15]): the constant-property baseline,

$$\mathrm{Nu}_b = 0.023\,\mathrm{Re}_b^{0.8}(T)\,\mathrm{Pr}_b^{0.4}(T). \tag{7}$$

   No property-ratio correction is applied; deviations from this model quantify the magnitude of variable-property effects.

2. **LinP** (linearised pathway, Eq. (2)):

$$\mathrm{Nu}_b = C\,\sqrt{\mathrm{Re}_b(T)}\,\mathrm{Pr}_b^{-0.5}(T)\,\left(\frac{\mathrm{Pr}_b(T)}{\mathrm{Pr}_w(T)}\right)^{0.25}, \tag{8}$$

   with $C = 1$, $\beta = 0.5$, and $w\beta = 0.25$, all uncalibrated. The Prandtl ratio $\mathrm{Pr}_b/\mathrm{Pr}_w$ acts as a sublayer impedance correction without invoking the modified Prandtl number.

   The value $C = 1$ not only provides a clear improvement, but also confirms the penetration scaling $\mathrm{Nu} \approx \sqrt{\mathrm{Re}}$. Crucially, this single uncalibrated constant performs well for both water ($P/P_c = 1.065$) and CO_2 ($P/P_c = 1.22$), spanning reduced pressures from near-critical to moderately supercritical, Reynolds numbers from 7×10^4 to 2×10^6, and Prandtl numbers from 0.8 to 14. If the $\mathrm{Re}^{1/2}$ exponent were incorrect, no single value of C could accommodate fluids with such significantly different thermodynamic properties.

   The order-of-unity value of C is not merely an empirical convenience but a structural consequence of the $\mathrm{Re}^{1/2}$ exponent. To see this, consider the uncalibrated Dittus–Boelter correlation ($\mathrm{Nu}_b = \mathrm{Re}_b^{0.8}(T)\,\mathrm{Pr}_b^{0.4}(T)$) evaluated locally at the axial-position bulk temperature: at $\mathrm{Re}_b = 10^4$ and $\mathrm{Pr} \sim 1$, this gives $\mathrm{Nu} \approx 1585$, larger than the calibrated value ($\mathrm{Nu} \approx 36$) by a factor of ~ 43, driving $T_w \to T_b$ for any realistic heat flux. The calibrated prefactor 0.023 in the Dittus–Boelter equation (7) is small precisely because it must compensate for the steep $\mathrm{Re}^{0.8}$ growth, absorbing the gap between the log-law friction structure and a pure power law. By contrast, $\mathrm{Nu} = 1 \times (10^4)^{0.5} = 100$ is already in the correct physical range – a factor of two to three above the calibrated Dittus–Boelter value. The penetration scaling explains why: the Reynolds factor $f(\mathrm{Re}) = d/\delta_{\mathrm{pen}}$ of (73) (Part I) is a geometric ratio with an $O(1)$ prefactor by construction, and the pathway conductance bracket that multiplies it is itself $O(1)$ at $\mathrm{Pr} \sim 1$; no small empirical constant is needed because the $\mathrm{Re}^{1/2}$ exponent already matches the physical magnitude of the heat transfer. The prefactor $C \approx 1$ is connected to $n \approx 1/2$. This is demonstrated directly in the Q-mode wall temperature predictions of Section 3.4, where the uncalibrated Dittus–Boelter correlation ($\mathrm{Nu}_b = \mathrm{Re}_b^{0.8}(T)\,\mathrm{Pr}_b^{0.4}(T)$) is included alongside the pathway and other correlations for all cases. The comparison is instructive because the bulk

Reynolds number increases significantly along the heated length for nearly all cases (driven by the large viscosity decrease across the pseudocritical region), while the behaviour of the Prandtl number differs qualitatively: Pr_b increases or decreases significantly along the pipe reflecting the different thermodynamic trajectories relative to the c_p peak. Despite this contrasting evolution of the Prandtl-number, the uncalibrated Dittus–Boelter correlation with $\mathrm{Re}^{0.8}$ collapses T_w onto T_b uniformly in all cases, confirming that the chosen exponent, and not the differing thermodynamic properties, is the origin of the overprediction.

3. **Bishop** ([9]):

$$\mathrm{Nu}_b = 0.0069\,\mathrm{Re}_b^{0.9}(T)\,\overline{\mathrm{Pr}}_b^{0.66}(T)\left(\frac{\rho_w(T)}{\rho_b(T)}\right)^{0.43}, \tag{9}$$

where $\overline{\mathrm{Pr}}_b = \bar{c}_p\,\mu_b/\lambda_b$ uses the integrated mean specific heat $\bar{c}_p = (h_w - h_b)/(T_w - T_b)$. This is one of the best-performing correlations in Q-mode engineering practice [16–18] to mention a few. The explicit entrance-length factor of the original Bishop correlation (57) (Part I) is omitted here.

4. **Swenson** ([10]):

$$\mathrm{Nu}_w = 0.00459\,\mathrm{Re}_w^{0.923}(T)\,\overline{\mathrm{Pr}}_w^{0.613}(T)\left(\frac{\rho_w(T)}{\rho_b(T)}\right)^{0.231}, \tag{10}$$

where $\mathrm{Re}_w = G\,d/\mu_w$ and $\overline{\mathrm{Pr}}_w = \bar{c}_p\,\mu_w/\lambda_w$. The wall-evaluated formulation absorbs the Prandtl-ratio correction but introduces increased circularity (Section 5.3 (Part I)).

The four correlations span the main structural families identified in Section 4 (Part I): uncorrected baseline (DB), disentangled pathway with $\sqrt{\mathrm{Re}}$ scaling (LinP), entangled modified-Prandtl with density ratio (Bishop) and wall-evaluated with density ratio (Swenson). All correlations are computed locally as temperature and pressure dependent.

The uncalibrated Dittus–Boelter form $\mathrm{Nu}_b = \mathrm{Re}_b^{0.8}\,\mathrm{Pr}_b^{0.4}$ (denoted DBs) is carried along with the four correlations only as a diagnostic, not as a competing model: its role is to verify the $\mathrm{Re}^{0.8}\times 0.023$ entanglement derived analytically in [2].

3.4 Results

The comparison between LinP and the two entangled correlations is arranged as a three-point test along the entanglement axis of the general form (1). Bishop evaluates its Reynolds and modified Prandtl numbers at the bulk state, $\mathrm{Re}_b(T)$ and $\overline{\mathrm{Pr}}_b = \bar{c}_p\,\mu_b/\lambda_b$, and carries a density ratio $(\rho_w/\rho_b)^{0.43}$. Swenson evaluates the same entangled combination at the wall, $\mathrm{Re}_w(T)$ and $\overline{\mathrm{Pr}}_w = \bar{c}_p\,\mu_w/\lambda_w$, and carries $(\rho_w/\rho_b)^{0.231}$. The two correlations thereby realise the bulk-anchored and wall-anchored limits of the entangled, density-corrected architecture. LinP occupies the symmetric interior point: the two thermodynamic states enter the parallel conductance bracket of Eq. (61) (Part I) with equal weights $w = 1/2$, the unique unbiased assignment of the two-point quadrature (Eq. (79) (Part I)), and no density ratio is carried. Dittus–Boelter is retained as the uncorrected baseline.

The three-point comparison is diagnostic rather than a contest of accuracy. The purpose is to test whether the leading-order pathway analysis of Section 6 (Part I) – symmetric weighting, resistance exponent $\beta = 1/2$, no higher-order corrections – suffices to resolve the structural pathology that any one-sided entanglement must reproduce when the pseudocritical barrier sweeps through the boundary layer. LinP enters the comparison constrained by construction: it carries neither a fitted coefficient nor a density correction, whereas Bishop and Swenson retain their originally published exponents and include the multiplicative $(\rho_w/\rho_b)^r$ term that LinP deliberately omits.

Here *calibrated* is used in the operational sense standard in the supercritical Nusselt literature – the T-mode or Q-mode refitting of C and β to a target dataset, as in [19], which retains the Bishop structure but is refitted exclusively on supercritical water data. In this sense, LinP carries no calibrated parameters: $C = 1$ is adopted uncalibrated (C of order unity by construction), $w = 1/2$ is the unbiased assignment (79) (Part I), and $\beta = 1/2$ is fixed a priori in §6.1.5 (Part I) from the Mikheev–Žukauskas correlation family, consistent with the theoretical bounds $\beta \in (0, 2/3)$ of Section 3.2.3 (Part I). DB, Bishop and Swenson retain their originally published coefficients.

The predictions of the pathway analysis are tested against the experimental $T_w(x)$ in two tiers. An integrated metric, the Q-mode root-mean-square error of the predicted wall temperature per case, Table 7, quantifies the overall magnitude of each correlation's departure from the experiment. The axial behaviour of the predicted $T_w(x)$ profiles, examined case by case thereafter, carries the structural content. The distinction matters: an integrated metric necessarily conceals the axial distribution of the misprediction, and the signature the framework predicts – the reappearance of the spatial mismatch of Section 1.1(2) (Part I) in each one-sided correlation – is axial in character. The two subsections below specialise this assessment to the Reynolds-exponent prediction (§3.5) and the disentangled Prandtl-correction prediction (§3.6).

The dataset roles are:

- Grabezhnaya and Kirillov [5] water (Re-exponent): Re_b ratio 2.3–3.0 at moderate Pr_b variation (Table 10).
- JIHTRAS CO_2 (cross-fluid Re-exponent and HTD limit): $\mathrm{Re}_b \sim 10^6$ with Pr_b *decreasing* along the pipe, opposite to water, and strong-variation of HTD (Table 4). Upflow-downflow equivalent pairs.
- NTUU water [3, 4] (Prandtl correction): Pr_b grows from 1.7 to 14 over a short heated length (Table 9).
- Yamagata et al. [6] water (horizontal, increasing and decreasing Prandtl numbers): pre- and post-crossing entries.
- NTUU downflow #104, #145 (buoyancy limit): buoyancy opposes the mean flow.

Table 7 reports the root-mean-square error of the wall-temperature in the Q-mode, $\mathrm{RMS}(T_w^{\mathrm{pred}} - T_w^{\mathrm{exp}})$ in kelvin, for each of the eighteen cases and each of the four correlations, evaluated at the experimental axial locations $N_{\mathrm{sta.}}$. The predicted profiles are obtained by iterative convergence of T_w from the prescribed heat flux (Section 3.1); no correlation is recalibrated. All results reported below are computed at axial resolution $N = 1000$ and iteration tolerance 10^{-4}; halving the tolerance and reducing the segment count both leave the predicted $T_w(x)$ profiles unchanged to the plotting precision.

Across the eighteen cases LinP carries the lowest case-mean RMS at 31.5 K, against 47.9 K for Bishop, 54.3 K for Swenson and 55.1 K for Dittus–Boelter – a reduction of 34–43% relative to the three comparators, obtained with neither a fitted coefficient nor a density correction. LinP is the best model in nine of the eighteen cases; Swenson in six, DB in two, Bishop in one. The nine residual cases separate into three subsets examined downstream: the JIHTRAS HTD peaks #44 and #45, where the wall-to-bulk density contrast dominates the heat transfer; the NTUU downflow case #145, where buoyancy leaves the forced-convection scope of the leading-order analysis; and six

Dataset	Case	q_w/G (J/kg)	$N_{\text{sta.}}$	DB	LinP	Bishop	Swenson
NTUU (upflow)	#555	825	16	49.6	**5.8**	35.9	27.1
NTUU (upflow)	#565	948	16	69.1	**13.7**	44.6	43.7
NTUU (upflow)	#574	1074	13	105.9	**43.2**	69.7	46.4
NTUU (upflow)	#583	1155	10	101.7	**40.6**	57.7	66.2
NTUU (downflow)	#104	1576	15	78.1	**38.4**	43.6	176.5
NTUU (downflow)	#145	2056	12	**22.0**	42.2	175.1	317.6
Kirillov (upflow)	53	799	112	76.3	41.5	65.7	**24.0**
Kirillov (upflow)	54	496	81	15.3	19.7	14.7	**6.8**
Kirillov (upflow)	58	680	81	29.5	**8.7**	24.2	16.8
Kirillov (upflow)	62	466	79	10.4	6.7	11.2	**6.2**
Yamagata (horizontal)	111	554	9	6.7	17.6	11.5	**5.6**
Yamagata (horizontal)	112	554	9	**5.5**	14.6	12.0	7.3
Yamagata (horizontal)	121	738	9	23.1	18.0	**12.3**	35.7
Yamagata (horizontal)	122	738	9	46.0	**8.7**	33.9	16.6
JIHTRAS (upflow)	42	204	21	127.0	**59.1**	96.9	75.0
JIHTRAS (upflow)	44	193	13	64.1	71.0	42.7	**30.3**
JIHTRAS (downflow)	43	204	16	97.1	**41.3**	65.3	42.7
JIHTRAS (downflow)	45	193	11	64.0	76.7	44.8	**33.0**
Mean across cases				55.1	**31.5**	47.9	54.3

Table 7: Q-mode wall-temperature root-mean-square error RMS($T_w^{\text{pred}} - T_w^{\text{exp}}$) in K per case × model, evaluated at the $N_{\text{sta.}}$ experimental axial locations. Predicted profiles are obtained by iterative convergence of T_w from the prescribed heat flux (Section 3.1). No correlation is recalibrated. Bold entries mark the best model per case.

moderate-variation or pre-crossing entries (Kirillov #53, #54, #62; Yamagata #111, #112, #121), discussed alongside the crossing-active cases of the same datasets in §3.5 and §3.6.

The Kelvin-valued residual of Table 7 carries a unit artefact across fluids: a 30 K departure on a water case ($T_w^{\text{exp}} \sim 670$ K) and the same 30 K departure on a CO_2 case ($T_w^{\text{exp}} \sim 320$ K) report identically in kelvin yet represent differently scaled fractions of the local heat-transfer process. Table 8 normalises the residual by the per-case mean wall-to-bulk driving difference,

$$\overline{\Delta T_{wb}} = \frac{1}{N_{\text{sta.}}} \sum_{i=1}^{N_{\text{sta.}}} \left[T_w^{\text{exp}}(x_i) - T_b^{\text{exp}}(x_i)\right], \tag{11}$$

i.e. the case-averaged q_w/α_{exp} that each correlation attempts to predict. The experimental bulk temperature T_b^{exp} is replaced by the calculated value in cases where the experimental results are not provided. Both tables lead to the same conclusions: the results are preserved case-by-case, LinP remains the best model on the same nine of eighteen cases, with lowest case-mean error at 36.8%, against 58.3% for DB, 52.0% for Bishop, and 56.7% for Swenson. The rescaling adds the per-case driving scale that the result in Kelvin suppresses: $\overline{\Delta T_{wb}}$ ranges from ~ 24 K (Kirillov #62) to ~ 154 K (JIHTRAS #42), so a Kelvin residual that reads modestly on a strongly driven case can represent a fractional departure comparable to a smaller residual on a weakly driven case.

The case-mean figure is a necessary condition for the framework: a correlation that failed to reduce the integrated error relative to the three comparators would not warrant a structural defence. It is not a sufficient one. The root-mean-square metric is a scalar summary of an axial distribution, whereas the pathology the framework predicts – the reappearance of the spatial mismatch of Section 1.1(2) (Part I) in each one-sided correlation, attenuated but not cured by the accompanying

Dataset	Case	q_w/G (J/kg)	$N_{\text{sta.}}$	$\overline{\Delta T_{wb}}$ (K)	DB	LinP	Bishop	Swenson
NTUU (upflow)	#555	825	16	73.1	67.9	**7.9**	49.2	37.1
NTUU (upflow)	#565	948	16	92.8	74.4	**14.8**	48.0	47.0
NTUU (upflow)	#574	1074	13	132.8	79.7	**32.5**	52.5	35.0
NTUU (upflow)	#583	1155	10	136.4	74.5	**29.8**	42.3	48.5
NTUU (downflow)	#104	1576	15	106.4	73.4	**36.1**	41.0	165.9
NTUU (downflow)	#145	2056	12	104.7	**21.0**	40.3	167.3	303.5
Kirillov (upflow)	53	799	112	106.4	71.7	39.0	61.7	**22.5**
Kirillov (upflow)	54	496	81	30.9	49.4	64.0	47.6	**22.1**
Kirillov (upflow)	58	680	81	57.8	51.0	**15.0**	41.8	29.1
Kirillov (upflow)	62	466	79	23.5	44.0	28.6	47.6	**26.4**
Yamagata (horizontal)	111	554	9	45.0	14.8	39.1	25.5	**12.4**
Yamagata (horizontal)	112	554	9	43.2	**12.7**	33.7	27.7	16.9
Yamagata (horizontal)	121	738	9	44.8	51.6	40.2	**27.6**	79.7
Yamagata (horizontal)	122	738	9	67.1	68.6	**12.9**	50.6	24.8
JIHTRAS (upflow)	42	204	21	153.7	82.7	**38.5**	63.1	48.8
JIHTRAS (upflow)	44	193	13	94.4	67.9	75.2	45.3	**32.1**
JIHTRAS (downflow)	43	204	16	134.5	72.2	**30.7**	48.6	31.8
JIHTRAS (downflow)	45	193	11	90.2	71.0	85.0	49.6	**36.6**
Mean across cases					58.3	**36.8**	52.0	56.7

Table 8: Q-mode wall-temperature root-mean-square error normalised by the per-case mean wall-to-bulk driving difference defined in Eq. (11), reported in percent. The denominator $\overline{\Delta T_{wb}}$ is the per-case average of the experimental wall temperature minus the energy-balance bulk temperature, taken over the $N_{\text{sta.}}$ experimental axial locations and shown in column 5; it is independent of the friction model. Predicted T_w profiles are obtained by iterative convergence from the prescribed heat flux (Section 3.1). No correlation is recalibrated. Bold entries mark the best model per case.

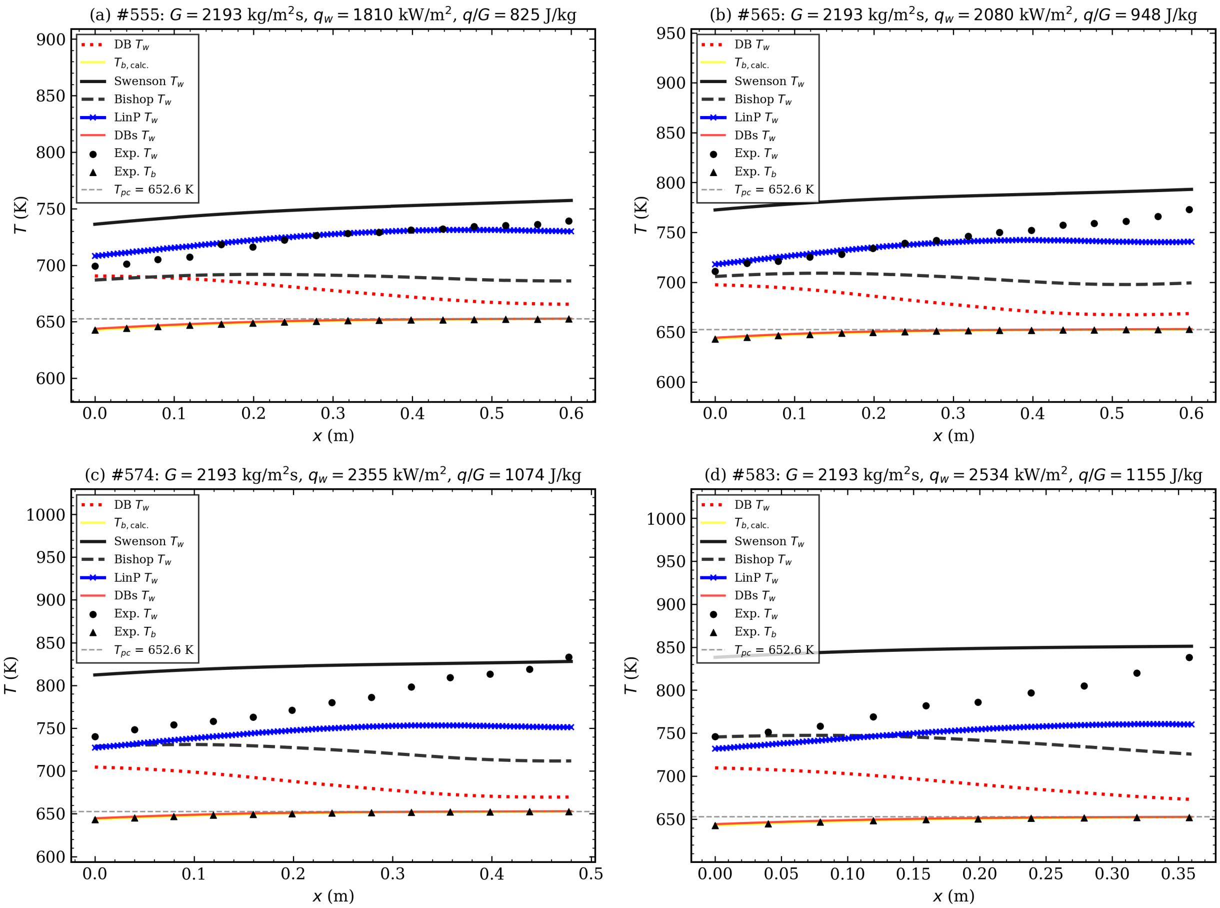

Figure 7: Predicted and experimental wall temperature profiles for the four NTUU supercritical water upflow cases (Table 2). Increasing heat flux from Case 1 (#555, $q_w/G = 825\,\mathrm{J/kg}$) to Case 4 (#583, $q_w/G = 1155\,\mathrm{J/kg}$).

density ratio – is axial in character. The case-by-case examination in the subsubsections that follow therefore carries the structural content of the comparison.

3.5 The Reynolds-number exponent

The penetration scaling of Section 6.1.4 (Part I) predicts $\mathrm{Nu} \sim \sqrt{\mathrm{Re}}$ in the barrier-dominated regime, against the $\mathrm{Re}^{0.8}$ of Dittus–Boelter and the $\mathrm{Re}/\ln \mathrm{Re}$ of the fully developed Lyon integral [2]. Two configurations isolate the exponent from the Prandtl correction. The Grabezhnaya and Kirillov [5] water cases span $\mathrm{Re}_{b,\mathrm{out}}/\mathrm{Re}_{b,\mathrm{in}} \approx 2.3$–$3.0$ at moderate Pr_b variation, giving the largest lever arm on the exponent within a single pipe. The JIHTRAS CO_2 cases at $\mathrm{Re}_b \sim 10^6$ carry a Pr_b evolution opposite to water, so an exponent preference that survives the sign reversal cannot be a disguised Prandtl effect.

On all cases the uncalibrated form $\mathrm{Nu}_b = \mathrm{Re}_b^{0.8}\,\mathrm{Pr}_b^{0.4}$ (DBs) collapses the predicted T_w onto T_b, demonstrating that the 0.023 prefactor is the structural compensation for the $\mathrm{Re}^{0.8}$ overshoot, not a gentle miscalibration, and confirming the analytical result of [2].

The **Grabezhnaya and Kirillov [5]** (GK) cases probe the Re-exponent in long heated pipes ($L = 4\,\mathrm{m}$) at moderate Prandtl variation and provide the strongest axial lever arm in the database,

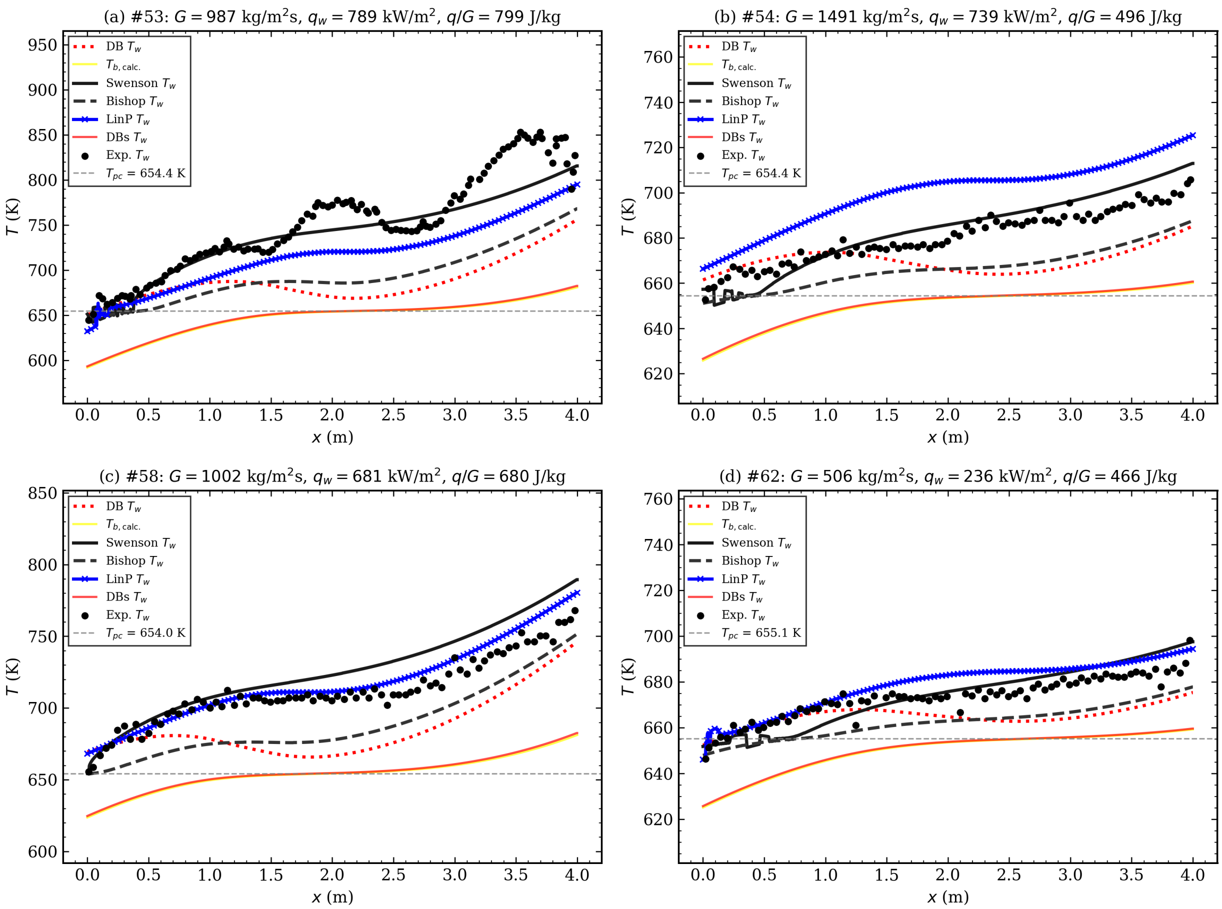

Figure 8: Predicted and experimental wall temperature profiles for the four supercritical water cases [5] (Table 5).

	Inlet	Outlet	Bulk avg.
#555: $q_w \approx 1810\,kW/m^2$, $q/G = 825\ J/kg$			
Re_b	226 678	341 680	279 893
Pr_b	1.73	14.28	6.51
$\mathrm{Nu}_{\mathrm{DB}}$	552	1781	1077
$\mathrm{Nu}_{\mathrm{LinP}}$	415	303	354
$\mathrm{Nu}_{\mathrm{Bishop}}$	165	205	187
$\mathrm{Nu}_{\mathrm{Swenson}}$	142	129	141

	Inlet	Outlet	Bulk avg.
#565: $q_w \approx 2080\,kW/m^2$, $q/G = 948\ J/kg$			
Re_b	228 225	365 496	291 778
Pr_b	1.78	12.72	7.61
$\mathrm{Nu}_{\mathrm{DB}}$	560	1794	1191
$\mathrm{Nu}_{\mathrm{LinP}}$	418	325	350
$\mathrm{Nu}_{\mathrm{Bishop}}$	150	204	175
$\mathrm{Nu}_{\mathrm{Swenson}}$	134	131	133

	Inlet	Outlet	Bulk avg.
#574: $q_w \approx 2355\,kW/m^2$, $q/G = 1074\ J/kg$			
Re_b	228 746	351 036	285 481
Pr_b	1.79	14.03	7.10
$\mathrm{Nu}_{\mathrm{DB}}$	563	1807	1135
$\mathrm{Nu}_{\mathrm{LinP}}$	420	312	354
$\mathrm{Nu}_{\mathrm{Bishop}}$	139	179	160
$\mathrm{Nu}_{\mathrm{Swenson}}$	129	120	128

	Inlet	Outlet	Bulk avg.
#583: $q_w \approx 2534\,kW/m^2$, $q/G = 1155\ J/kg$			
Re_b	226 678	319 831	269 967
Pr_b	1.73	12.24	5.14
$\mathrm{Nu}_{\mathrm{DB}}$	552	1588	956
$\mathrm{Nu}_{\mathrm{LinP}}$	423	310	370
$\mathrm{Nu}_{\mathrm{Bishop}}$	131	161	149
$\mathrm{Nu}_{\mathrm{Swenson}}$	125	118	127

Table 9: Characteristic dimensionless numbers for the NTUU supercritical water cases. Re_b and Pr_b are identical across models. Here and in Tables 10–12, the bulk-averaged Pr_b can exceed both endpoint values because Pr_b peaks at the interior pseudocritical crossing.

$\mathrm{Re}_{b,\mathrm{out}}/\mathrm{Re}_{b,\mathrm{in}} \approx 2.3$–$3.0$ (Table 10). The four regimes sample distinct wall-state trajectories relative to the pseudocritical temperature. In #53, #54 and #62 the wall enters well below T_{pc} and passes through it inside the pipe; in #58 the wall enters essentially at $T_w \approx T_{pc}$. The bulk enters below T_{pc} in every case and crosses it within the heated length at $x/L \approx 0.4$–0.6, so the four cases exhibit the prototypical spatial-mismatch problem of Section 1.1(2) (Part I) – wall and bulk traversing the barrier at different axial positions – over distances long enough for the $\sqrt{\mathrm{Re}}$ and $\mathrm{Re}^{0.8}$ predictions to separate by more than a factor of two.

Three of the four regimes – #53, #58 and #62 – follow the three-point ordering of the bulk-, symmetric- and wall-anchored correlations. Bishop underpredicts T_w in the $T_b \to T_{pc}$ region ($x/L \in [0.4, 0.6]$) and traces a $T_w(x)$ profile closely parallel to Dittus–Boelter throughout, confirming that the $(\rho_w/\rho_b)^{0.43}$ factor attenuates but does not cure the bulk-anchored Prandtl-entanglement pathology. Swenson underpredicts T_w in the upstream region where T_w crosses T_{pc} and then produces a nearly flat profile whose slope reflects the wall-state insensitivity to the bulk crossing; on #53 and #62 the flat profile happens to intersect the measured T_w closely enough that Swenson carries the lowest case RMS (Table 7). LinP reproduces both the inlet-region correction where T_w passes T_{pc} – an axial jump absent from both the DB and Bishop profiles – and the slope through the bulk crossing. Case #58, where the wall enters at T_{pc} and the inlet correction is therefore sharpest, is quantitatively cleanest: LinP reproduces the measured $T_w(x)$ to within the experimental scatter across the entire pipe (case RMS 8.7 K, lowest among the four correlations). On #53 and #62 the LinP slope matches the data but sits systematically below Swenson's profile by ∼20 K, producing RMS values (41.5 and 6.7 K respectively) that lie between Bishop's and Swenson's in the expected ordering.

Case #53 also exhibits an axial modulation of the measured T_w in the downstream three-quarters of the pipe, $x/L \in [0.25, 1.0]$: three local maxima and two local minima of amplitude $\sim$15 K and wavelength $\sim$0.5 m, superposed on a monotonic recovery trend. The pattern is distinct from the canonical single-peak M-profile associated with isolated heat-transfer deterioration and suggests a mechanism that repeats along the pipe rather than one tied to a single barrier crossing. No pointwise correlation in the comparison resolves this modulation, nor can one: the reference-temperature architecture samples properties at (T_b, T_w, P) station by station and carries no mechanism by which turbulent transport in a long heated pipe can support an axial oscillation of the wall-to-bulk impedance. RANS closures with a constant turbulent Prandtl number face the same structural limit. What the comparison does show is that Swenson and LinP each track the mean of the modulated profile – RMS 24.0 K and 41.5 K respectively – with an offset between them of $\sim$20 K. Neither correlation resolves the modulation; both predict the quantity they are designed to predict, namely the axial evolution of the mean wall-to-bulk impedance, and the $\sim$20 K offset between them lies within the envelope of the wall-evaluation and density-ratio effects that LinP does not carry. Case #53 therefore delimits the scope of the pointwise framework from above: where the mean impedance can be predicted by a reference- temperature correlation, it is; where an axial turbulence-mechanism modulation is superposed, it is not, and neither the leading-order pathway form of LinP nor the fully entangled, density-corrected forms of Bishop and Swenson can recover it. Resolving the modulation requires the full impedance integral (23) (Part I) with a variable turbulent Prandtl number $\mathrm{Pr}_t(r, T)$ and, likely, a direct numerical or wall-resolved large-eddy simulation, as identified in §4.

Case #54 is structurally distinct and interrogates rather than confirms the three-point ordering. Here LinP follows the axial trend of the measured T_w faithfully but overpredicts systematically by $\sim$20 K throughout the pipe – and, uncharacteristically, sits above not only Bishop and DB but also Swenson. The regime is the weakest in wall-to-bulk property contrast of the four GK cases: the highest mass flux ($G = 1491\,\mathrm{kg/(m^2\,s)}$) and the lowest q_w/G (496 J/kg) of the quartet, with $\mathrm{Pr}_b = 1.09$ at the inlet rising only to 3.45 at outlet (Table 10). In this weak-Prandtl-ratio regime the entangled correlations are depressed relative to the disentangled baseline through the same $\overline{\mathrm{Pr}}_b^{0.66}$ and $\overline{\mathrm{Pr}}_w^{0.613}$ exponents that over-respond to the c_p-driven Prandtl amplification at larger contrast. LinP, anchored on $\mathrm{Pr}_b^{-1/2}(\mathrm{Pr}_b/\mathrm{Pr}_w)^{1/4}$ with $\beta = 1/2$ fixed by the external-empirical prior of Section 6.1.5 (Part I), carries no such depression. The inversion of the three-point order in #54 is therefore consistent with the bracket function $\mathcal{F}_{\mathrm{exp}}$ departing above the parallel envelope in the moderate-ξ region of Figure 4(b), where the measured $\mathcal{F}$ lies above $\mathcal{F}_{\mathrm{LinP}}$; LinP is the first-order form and does not carry the θ_{pc}-structured correction the envelope analysis has already identified as necessary.

The **JIHTRAS CO_2 cases** [7, 8] at $P/P_c = 1.22$ operate an order of magnitude above the water datasets, $\mathrm{Re}_b \sim 9\times10^5$–$2\times10^6$ (Table 11), and carry Pr_b *decreasing* along the pipe – opposite to the NTUU and GK water datasets, where Pr_b rises as T_b approaches T_{pc}. DB overpredicts Nu_b throughout under both Prandtl trajectories (DB RMS 64–127 K, Table 7). The $\mathrm{Re}^{0.8}$ overshoot is therefore structural, not an artefact of a particular Prandtl landscape.

3.6 The Prandtl correction and the entanglement artefact

The pathway analysis predicts that the Prandtl correction should enter through the ratio $\mathrm{Pr}_b/\mathrm{Pr}_w$ (Eq. (2)), not through the modified Prandtl number $\overline{\mathrm{Pr}}_b = \bar{c}_p\,\mu_b/\lambda_b$, which entangles the eliminable $\bar{c}_p/c_{p,b}$ artefact with the physical sublayer–barrier balance (Section 3.1 (Part I)). The entanglement causes $\overline{\mathrm{Pr}}_b$ to diverge as $T_b \to T_{pc}$ (because $\bar{c}_p$ inherits the c_p peak), whereas the physical correction $\mathrm{Pr}_b/\mathrm{Pr}_w$ remains bounded.

The **NTUU** water upflow cases [3, 4] isolate the Prandtl correction in a particularly clean

	Inlet	Outlet	Bulk avg.
#53: $G = 987\,kg/(m^2\,s)$, $q_w = 789\,kW/m^2$			
Re_b	116 779	351 192	234 403
Pr_b	0.87	1.89	3.82
$\mathrm{Nu}_{\mathrm{DB}}$	246	811	745
$\mathrm{Nu}_{\mathrm{LinP}}$	318	505	355
$\mathrm{Nu}_{\mathrm{Bishop}}$	132	517	261
$\mathrm{Nu}_{\mathrm{Swenson}}$	102	383	176

	Inlet	Outlet	Bulk avg.
#54: $G = 1491\,kg/(m^2\,s)$, $q_w = 739\,kW/m^2$			
Re_b	210 185	491 943	341 648
Pr_b	1.09	3.45	5.09
$\mathrm{Nu}_{\mathrm{DB}}$	432	1350	1152
$\mathrm{Nu}_{\mathrm{LinP}}$	416	500	391
$\mathrm{Nu}_{\mathrm{Bishop}}$	271	626	390
$\mathrm{Nu}_{\mathrm{Swenson}}$	202	396	246

	Inlet	Outlet	Bulk avg.
#58: $G = 1002\,kg/(m^2\,s)$, $q_w = 681\,kW/m^2$			
Re_b	139 487	357 442	259 215
Pr_b	1.07	1.87	4.45
$\mathrm{Nu}_{\mathrm{DB}}$	308	818	849
$\mathrm{Nu}_{\mathrm{LinP}}$	340	507	358
$\mathrm{Nu}_{\mathrm{Bishop}}$	172	565	318
$\mathrm{Nu}_{\mathrm{Swenson}}$	127	411	206

	Inlet	Outlet	Bulk avg.
#62: $G = 506\,kg/(m^2\,s)$, $q_w = 236\,kW/m^2$			
Re_b	70 921	160 978	111 728
Pr_b	1.08	4.07	4.87
$\mathrm{Nu}_{\mathrm{DB}}$	180	590	466
$\mathrm{Nu}_{\mathrm{LinP}}$	238	269	222
$\mathrm{Nu}_{\mathrm{Bishop}}$	125	243	165
$\mathrm{Nu}_{\mathrm{Swenson}}$	88	144	101

Table 10: Characteristic dimensionless numbers for the Grabezhnaya and Kirillov [5] supercritical water cases.

geometry. Across the four regimes #555–#583, the wall temperature remains thermodynamically stable throughout the heated length: the inlet-side T_w rises from ∼710 K to ∼750 K across the sequence as q_w/G grows from 825 to 1155 J/kg, so that $T_w - T_{pc}$ stays in the range 60–100 K and the wall-side properties are effectively frozen. The bulk, by contrast, enters at $T_{\mathrm{in}} \approx 643$ K (Table 2) and crosses T_{pc} near $x \approx 0.25\,L$; thereafter T_b plateaus in the immediate vicinity of T_{pc} under the influence of the c_p peak. This configuration – wall state fixed, bulk traversing the pseudocritical barrier once and remaining in its neighbourhood for three-quarters of the heated length – means that any axial variation in the predicted $T_w(x)$ must originate in how a correlation couples the wall to the bulk as T_b passes through T_{pc} and Pr_b rises from ∼1.7 to ∼14 (Table 9).

The Swenson and Bishop predictions exhibit, in opposite directions, the spatial-mismatch pathology (Section 1.1(2) (Part I)). Swenson, anchored entirely on the wall through Re_w and $\overline{\mathrm{Pr}}_w$, is structurally blind to the bulk crossing: the predicted $T_w(x)$ rises nearly linearly by only ∼20 K from inlet to outlet in each of the four cases, well within the 30–60 K scatter of a profile that happens to intersect the measured T_w near the outlet. The low case-mean RMS is the signature of a prediction axially insensitive to the barrier crossing rather than one that resolves it. Bishop, anchored on the bulk through Re_b and $\overline{\mathrm{Pr}}_b$, inherits the opposite pathology: as $T_b \to T_{pc}$ the integrated specific heat $\bar{c}_p$ enters the c_p peak and drives $\overline{\mathrm{Pr}}_b^{0.66}$ upward, pulling the predicted T_w down toward T_b along the same axial trajectory as Dittus–Boelter – the $(\rho_w/\rho_b)^{0.43}$ factor attenuates the descent but does not correct it. The two entangled correlations therefore realise the wall-locked and bulk-locked limits of the spatial mismatch; each is cured of the other's pathology and afflicted by its own, as the one-sided architecture requires.

LinP reproduces the axial response to the crossing without reproducing either pathology, and its graded accuracy across the four cases carries an independent physical reading. The prediction is

	Inlet	Outlet	Bulk avg.
#42 (upflow): $G = 2100\,kg/(m^2\,s)$, $q_w \approx 428\,kW/m^2$			
Re_b	918 717	2 016 375	1 476 399
Pr_b	3.84	2.39	4.62
$\mathrm{Nu}_{\mathrm{DB}}$	2322	3603	3564
$\mathrm{Nu}_{\mathrm{LinP}}$	730	1220	893
$\mathrm{Nu}_{\mathrm{Bishop}}$	867	1797	1223
$\mathrm{Nu}_{\mathrm{Swenson}}$	1007	1712	1204

	Inlet	Outlet	Bulk avg.
#43 (downflow): $G = 2100\,kg/(m^2\,s)$, $q_w \approx 428\,kW/m^2$			
Re_b	918 717	2 016 375	1 476 399
Pr_b	3.84	2.39	4.62
$\mathrm{Nu}_{\mathrm{DB}}$	2322	3603	3564
$\mathrm{Nu}_{\mathrm{LinP}}$	730	1220	893
$\mathrm{Nu}_{\mathrm{Bishop}}$	867	1797	1223
$\mathrm{Nu}_{\mathrm{Swenson}}$	1007	1712	1204

	Inlet	Outlet	Bulk avg.
#44 (upflow): $G = 2140\,kg/(m^2\,s)$, $q_w \approx 413\,kW/m^2$			
Re_b	922 642	1 993 215	1 456 529
Pr_b	3.75	2.70	4.76
$\mathrm{Nu}_{\mathrm{DB}}$	2308	3748	3593
$\mathrm{Nu}_{\mathrm{LinP}}$	736	1175	875
$\mathrm{Nu}_{\mathrm{Bishop}}$	896	1749	1223
$\mathrm{Nu}_{\mathrm{Swenson}}$	1034	1642	1199

	Inlet	Outlet	Bulk avg.
#45 (downflow): $G = 2140\,kg/(m^2\,s)$, $q_w \approx 413\,kW/m^2$			
Re_b	922 642	1 993 215	1 456 529
Pr_b	3.75	2.70	4.76
$\mathrm{Nu}_{\mathrm{DB}}$	2308	3748	3593
$\mathrm{Nu}_{\mathrm{LinP}}$	736	1175	875
$\mathrm{Nu}_{\mathrm{Bishop}}$	896	1749	1223
$\mathrm{Nu}_{\mathrm{Swenson}}$	1034	1642	1199

Table 11: Characteristic dimensionless numbers for the JIHTRAS supercritical CO_2 cases. Pairs #42/#43 and #44/#45 are matched-condition upflow/downflow experiments; bulk thermodynamics and predicted Nu are therefore identical within each pair.

	Inlet	Outlet	Bulk avg.
#111: $G = 1260\,kg/(m^2\ s)$, $q_w \approx 698\,kW/m^2$			
Re_b	103 519	149 965	124 459
Pr_b	0.83	1.47	1.02
$\mathrm{Nu}_{\mathrm{DB}}$	219	371	277
$\mathrm{Nu}_{\mathrm{LinP}}$	331	353	349
$\mathrm{Nu}_{\mathrm{Bishop}}$	100	133	114
$\mathrm{Nu}_{\mathrm{Swenson}}$	83	107	94

	Inlet	Outlet	Bulk avg.
#112: $G = 1260\,kg/(m^2\ s)$, $q_w \approx 698\,kW/m^2$			
Re_b	105 197	153 274	126 707
Pr_b	0.83	1.58	1.05
$\mathrm{Nu}_{\mathrm{DB}}$	223	389	284
$\mathrm{Nu}_{\mathrm{LinP}}$	333	351	350
$\mathrm{Nu}_{\mathrm{Bishop}}$	101	135	116
$\mathrm{Nu}_{\mathrm{Swenson}}$	84	109	95

	Inlet	Outlet	Bulk avg.
#121: $G = 1260\,kg/(m^2\ s)$, $q_w \approx 930\,kW/m^2$			
Re_b	176 462	317 867	253 505
Pr_b	2.87	2.79	5.61
$\mathrm{Nu}_{\mathrm{DB}}$	552	874	941
$\mathrm{Nu}_{\mathrm{LinP}}$	313	448	341
$\mathrm{Nu}_{\mathrm{Bishop}}$	126	297	186
$\mathrm{Nu}_{\mathrm{Swenson}}$	103	228	135

	Inlet	Outlet	Bulk avg.
#122: $G = 1260\,kg/(m^2\ s)$, $q_w \approx 930\,kW/m^2$			
Re_b	181 909	320 749	259 090
Pr_b	3.37	2.63	5.59
$\mathrm{Nu}_{\mathrm{DB}}$	603	861	952
$\mathrm{Nu}_{\mathrm{LinP}}$	306	457	347
$\mathrm{Nu}_{\mathrm{Bishop}}$	129	309	193
$\mathrm{Nu}_{\mathrm{Swenson}}$	104	240	141

Table 12: Characteristic dimensionless numbers for the Yamagata et al. [6] supercritical water cases. Re_b and Pr_b are identical across models.

essentially exact on #555 ($q_w/G = 825\,\mathrm{J/kg}$), becomes a slight underprediction on #565, and underpredicts with a deficit growing toward the outlet on #574 and #583 ($q_w/G = 1074$ and $1155\,\mathrm{J/kg}$). The axial trend slope remains correct in every case, however, the magnitude degrades with increasing q_w/G. This is the signature the framework predicts: the wall-to-bulk density contrast ρ_w/ρ_b grows with q_w/G, and the pathway-resolved density correction required to resolve ρ_w/ρ_{pc} and ρ_{pc}/ρ_b within each pathway (Section 6 (Part I)) is absent from the linearised form. The quartet #555–#583 accordingly traces the approach to the conductance upper bound as the variable-density contribution becomes non-negligible, and locates the quantitative limit of LinP in the same place the scaling analysis has located it a priori.

Figures 10a and 10b show the two **NTUU downflow** cases ($q_w/G = 1576$ and $2056\,\mathrm{J/kg}$; conditions in Table 3). Both cases operate outside the upflow regime that supplies most of the database and occupy the buoyancy-limited corner of the forced-convection scope. Case #104 ($G = 509\,\mathrm{kg/(m^2\,s)}$, $q_w = 802\,\mathrm{kW/m^2}$) exhibits a long bulk plateau: T_b enters at 640 K, rises to T_{pc} near the inlet and remains in the immediate vicinity of T_{pc} across $x/L \in [0.20, 0.87]$, sustained by the c_p peak against the imposed heat flux. The wall enters near T_{pc} and rises monotonically thereafter. Case #145 ($G = 248\,\mathrm{kg/(m^2\,s)}$, $q_w = 510\,\mathrm{kW/m^2}$) is structurally inverted: T_w enters well above T_{pc} and rises by $\sim$100 K along the pipe, while T_b rises linearly to approach $T_{pc} - 10\,\mathrm{K}$ at the outlet without crossing.

On #104, Swenson produces a strictly linear $T_w(x)$ profile rising from $\sim$920 to $\sim$940 K, insensitive to the long bulk plateau at T_{pc} – the wall-lock pathology that recurs on #121/#122 and on the JIHTRAS upflows discussed below, here exaggerated by the bulk's sustained residence at T_{pc}. Bishop enters overpredicting by $\sim$50 K, descends smoothly to match the experiment at $x/L \approx 0.47$, and tracks the data closely for $x/L > 0.47$: the bulk-anchored $\overline{\mathrm{Pr}}_b$ of Bishop, amplified by the sustained c_p peak of the plateau, drives the predicted T_w downward through the same mechanism seen on the NTUU upflow cases, but the plateau duration allows the descent to complete within the pipe rather than overshoot. LinP follows the experimental axial trend throughout but underpredicts by $\sim$30 K for $x/L > 0.67$, consistent with the deferred pathway-resolved density correction in the region where the plateau sustains the wall-to-bulk density contrast at its maximum; DB exhibits the spatial-mismatch pathology in the $T_b \approx T_{pc}$ region with a local T_w minimum that the experimental profile does not show.

Case #145 is the instructive case of the subsection: LinP ranks worse on the integrated metric but better on the behavioural signature. LinP underpredicts mildly for $x/L \lesssim 0.07$, develops a correction rising from $x/L \approx 0.07$ to a local maximum at $x/L \approx 0.125$ that matches the experimental T_w, falls just above T_{pc} at $x/L \approx 0.15$, and thereafter tracks the experimental T_w on a parallel axial slope with a systematic underprediction of $\sim$40 K to the outlet. The bump is the LinP response to the bulk approaching the barrier-dominated regime; its axial location and amplitude are correctly identified, and the parallel-slope downstream behaviour tracks the physics of the barrier-induced heat-transfer evolution. The residual $\sim$40 K offset is the same scope-limit signature seen on the JIHTRAS HTD peaks: the linearised form cannot quantitatively reach the measured T_w magnitude without the pathway-resolved ρ_w/ρ_b correction. Swenson overpredicts by $\sim$300 K on a strictly linear trajectory from 1000 to 1060 K, recalling the strong-overprediction signature documented by [20] for wall-evaluated correlations in downflow regimes with a sustained near-T_{pc} bulk. Bishop enters at 840 K, rises linearly to 920 K, and sits below the experiment by $\sim$100 K throughout – the bulk-anchored entanglement expressed in a regime where the bulk does not cross T_{pc} and the $\overline{\mathrm{Pr}}_b$ descent cannot be activated.

DB carries the lowest RMS on #145 (22.0 K, against LinP's 42.2 K) by a specific mechanism: the prediction overpredicts by $\sim$30 K for $x/L \lesssim 0.5$ and underpredicts by $\sim$40 K for $x/L \gtrsim 0.5$, and the two signed errors of comparable magnitude cancel in the integrated metric. The integrated

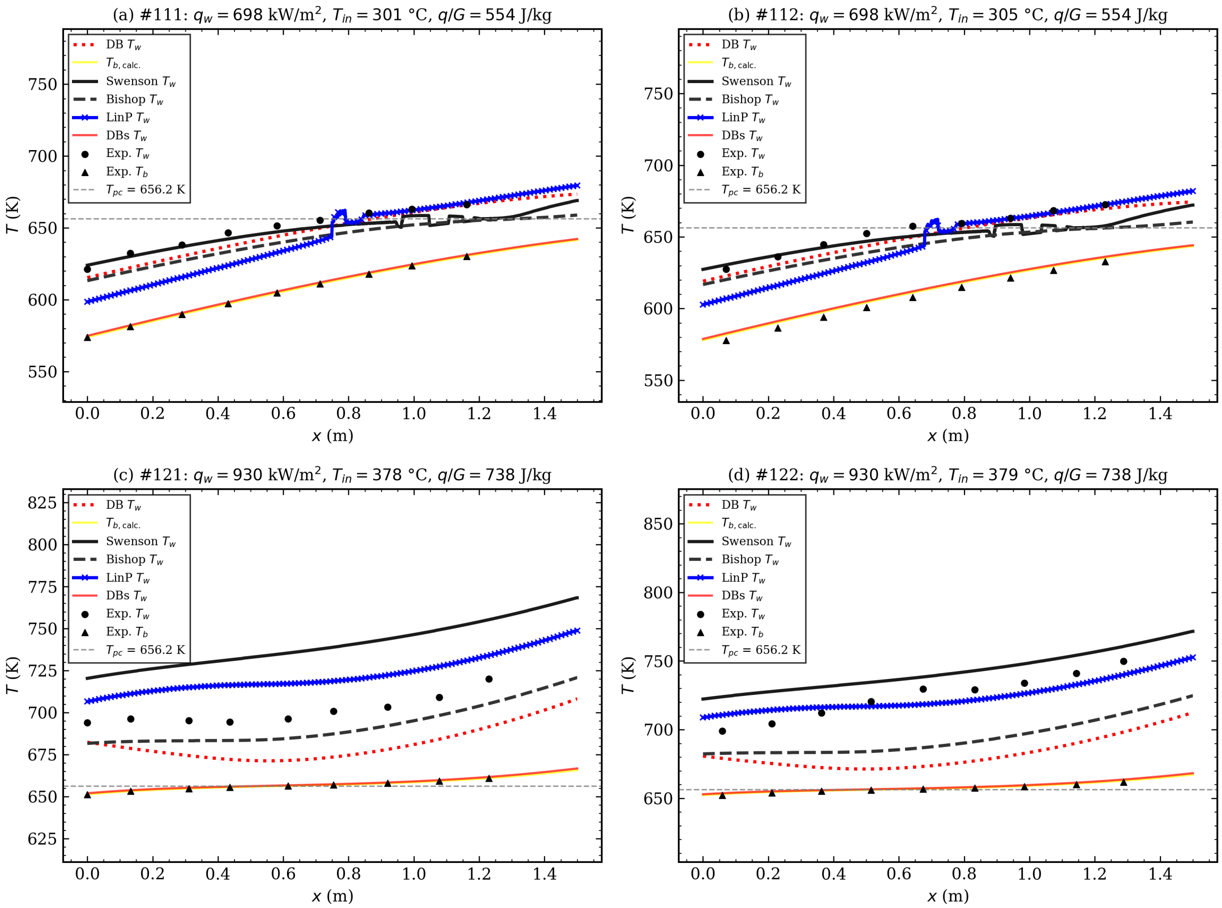

Figure 9: Predicted and experimental wall and bulk temperature profiles for the four Yamagata supercritical water cases (Table 6); #111/#121 bottom wall, #112/#122 top wall.

RMS therefore rewards a profile that bisects the data through axial insensitivity rather than one that tracks the data through axial responsiveness, and #145 is the database case where this distinction is cleanest. The LinP bump at $x/L \approx 0.125$ and the parallel-slope downstream match are the behavioural content the correlation is designed to deliver; the integrated metric, here, conceals that content under a same-magnitude cancellation. No symmetry or first-principles argument recommends the bisecting error distribution over the parallel-slope underprediction as an expression of the physics.

A numerical note: across all NTUU downflow cases and in the JIHTRAS post-crossing regions, the Swenson prediction exhibited weak oscillations as $T_w(x)$ crossed T_{pc}, arising from the axial discreteness of the iterative T_w-closure combined with the sharp wall-side property transition. At the axial resolution used throughout ($N = 1000$) these oscillations did not propagate into numerical instability and did not significantly affect the reported RMS values; at reduced resolution ($N = 500$) they grew in amplitude without altering the integrated metric by more than the plotting precision.

The **Yamagata et al. [6]** horizontal cases at $P = 24.5\,\text{MPa}$ provide the most informative behavioural test in the database because the experiment reports $T_b(x)$ alongside $T_w(x)$, so the energy-balance bulk trajectory can be verified independently. The pairs #111/#112 and #121/#122 are the bottom- and top-wall records of the same two runs: the $T_w(x)$ comparison uses the bottom

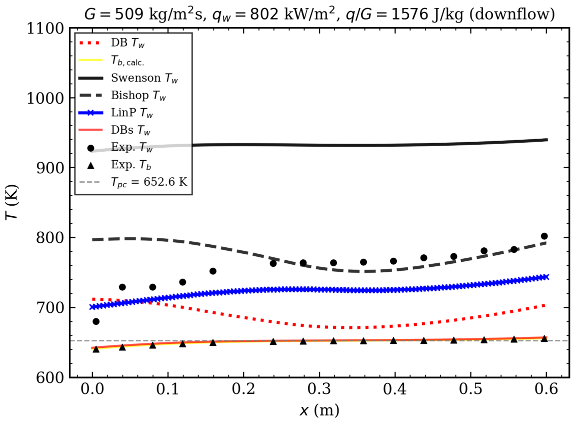

(a) NTUU downflow #104 ($G = 509\,\mathrm{kg/(m^2\,s)}$, $q_w = 802\,\mathrm{kW/m^2}$).

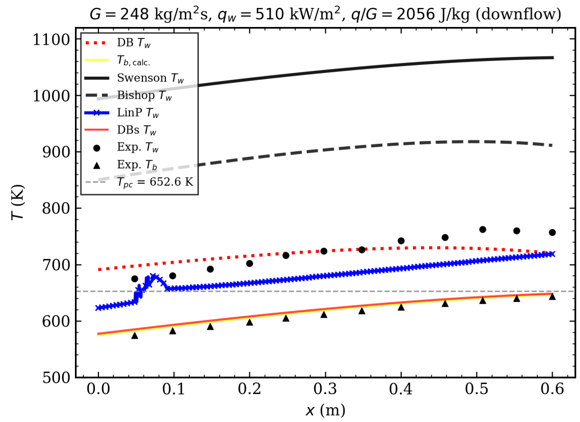

(b) NTUU downflow #145 ($G = 248\,\mathrm{kg/(m^2\,s)}$, $q_w = 510\,\mathrm{kW/m^2}$).

Figure 10: Predicted and experimental temperature profiles for NTUU downflow regimes.

wall for #111 and #121 and the top wall for #112 and #122. For horizontal supercritical flow the top wall carries the stronger buoyancy-induced deterioration, which is why the wall-side records of one run are treated as separate cases. In three of the four cases the VarTherm bulk prediction agrees with the measured T_b to within 0.5% over the entire pipe; on #112 the predicted $T_b(x)$ is shifted uniformly upward by $\sim$3 K relative to the measurement while preserving the profile shape, attributable to an inlet-enthalpy uncertainty. As in the other datasets, the DBs diagnostic collapses the predicted T_w onto T_b on all four cases [2].

The intermodel differences in $T_w(x)$ are therefore attributable to the Nusselt correlation alone. The four cases fall into two structurally opposite configurations: #111 and #112 enter with both wall and bulk below T_{pc} and the wall crosses T_{pc} inside the pipe at $x/L \approx 0.5$ while the bulk stays below; #121 and #122 enter with the wall stably above T_{pc} throughout and the bulk crossing T_{pc} at $x/L \approx 0.5$. The two configurations exchange the roles of wall and bulk with respect to the pseudocritical barrier and thereby probe the wall- and bulk-side limits of the correction architecture symmetrically.

On #111 and #112, for $x/L < 0.5$, the measured T_w crosses T_{pc} smoothly on a trajectory nearly parallel to the measured T_b. In this pre-crossing region Swenson tracks the data closely, DB and Bishop underpredict mildly, and LinP underpredicts by $\sim$20 K while retaining the correct axial slope. The Swenson advantage here has a direct structural reading: the wall state is well below T_{pc} and the wall-evaluated $\overline{\mathrm{Pr}}_w$ is neither entering nor traversing the c_p peak, so the wall-anchored entanglement is momentarily benign. As the wall approaches and crosses T_{pc} in the region $x/L \in [0.50, 0.57]$, LinP exhibits a damped cosine-like oscillation through the crossing – rising to a local maximum, descending through T_{pc}, rising again through T_{pc}, and settling smoothly – and matches the measured T_w to within the experimental scatter thereafter.

Swenson, for its part, develops a transient depression of predicted T_w through $x/L \in [0.60, 0.80]$ as the wall-evaluated $\overline{\mathrm{Pr}}_w$ follows the c_p peak directly; the predicted T_w drops toward Bishop's level before recovering toward the experiment for $x/L \gtrsim 0.87$. This excursion is the wall-side analogue of the Bishop bulk-side descent at $T_b \to T_{pc}$ observed throughout the rest of the database: an entangled $\overline{\mathrm{Pr}}$ following the c_p peak of the local reference state, attenuated but not cured by the accompanying density ratio. Bishop tracks the post-crossing trend with a systematic underprediction of comparable magnitude but without the transient excursion, since its reference state (bulk) remains well below

T_{pc} throughout.

On #121 and #122 the configuration is inverted. The wall state is stably above T_{pc} and the bulk crosses T_{pc} near $x/L \approx 0.5$. DB exhibits the canonical spatial-mismatch pathology through the $T_b \approx T_{pc}$ region. Bishop and LinP track the post-crossing trend of the experiment faithfully: LinP reproduces the measured $T_w(x)$ to within the experimental scatter on #122 (case RMS 8.7 K, Table 7), and sits in the expected interior position on #121 – slightly overpredicting where Swenson overpredicts strongly and Bishop slightly underpredicts, recovering the three-point ordering Bishop < LinP < Swenson that the symmetric-weight construction anticipates. Swenson in this configuration produces a strictly linear $T_w(x)$ profile, since the wall state sits stably above T_{pc} and the wall-evaluated reference properties are axially insensitive to the bulk crossing – the same wall-lock pathology observed in the JIHTRAS cases, here expressed as a smooth overprediction rather than an axial flattening. Bishop on #122 overpredicts slightly on an essentially linear profile, a mild variant of the same structural insensitivity.

The four Yamagata cases taken together complete the symmetry argument. In #121, #122 the bulk traverses T_{pc} and the bulk-anchored Bishop correlation inherits the $\overline{\mathrm{Pr}}_b$-through-c_p-peak pathology; Swenson, wall-anchored and insensitive to the bulk crossing, produces the linear wall-lock profile. In #111, #112 the wall traverses T_{pc} and the roles invert: Swenson inherits the wall-side analogue of the entangled descent as $\overline{\mathrm{Pr}}_w$ follows the c_p peak, while Bishop, bulk-anchored and with the bulk well below T_{pc}, tracks the trend benignly. The pathology is a property of *whichever* reference state passes through the pseudocritical temperature, not of the bulk state specifically; each one-sided entangled correlation suffers it when its own reference state makes the crossing. LinP, symmetric in wall and bulk by the $w = 1/2$ quadrature, and using the bounded $(\mathrm{Pr}_b/\mathrm{Pr}_w)^{1/4}$ factor rather than $\overline{\mathrm{Pr}}^m$, exhibits neither variant of the pathology: it responds to whichever crossing is active (#111, #112 through the wall-side jump, #121 and #122 through the bulk-side sustained correction) and does so at the interior point that the symmetry of the construction requires.

The **JIHTRAS $\mathbf{CO_2}$ cases** [7, 8] at $P/P_c = 1.22$ occupy the highest-Reynolds, strongest-density-contrast corner of the database: $\mathrm{Re}_b \sim 9\times10^5$–$2\times10^6$, with Pr_b *decreasing* along the pipe – opposite to the NTUU and GK water datasets. The wall temperature is stably above T_{pc} throughout, $T_w - T_{pc} \gtrsim 50\,\mathrm{K}$, while the bulk crosses T_{pc} linearly without forming the plateau observed in the NTUU upflow cases.

The four regimes are arranged as matched upflow/downflow pairs, #42/#43 and #44/#45, with identical bulk thermodynamics and therefore identical predicted $\mathrm{Nu}_b(x)$ within each pair; the intrapair differences in measured T_w are entirely orientation-driven, reflecting the known sensitivity of near-pseudocritical CO_2 to buoyancy modification of the near-wall turbulence below the conventional Ri threshold [12, 20].

On #42 and #44 (upflow), the diagnostic uncalibrated form DBs ($\mathrm{Nu}_b = \mathrm{Re}_b^{0.8}\mathrm{Pr}_b^{0.4}$, red) collapses the predicted T_w onto the energy-balance $T_b(x)$ trace (yellow) into a single orange line, directly exhibiting the prefactor–exponent entanglement established in [2]: the $\mathrm{Re}_b^{0.8}$ growth along the pipe (a factor of ∼2.2 between inlet and outlet, Table 11) drives $T_w \to T_b$ and the $\mathrm{Pr}_b^{0.4}$ term does not control it. DB, with the calibrated 0.023 prefactor that [2] shows to be the structural compensation for the $\mathrm{Re}^{0.8}$ overshoot, does not collapse: it underpredicts T_w by 60–110 K throughout and exhibits a local T_w minimum and reversed trend through the $T_b \approx T_{pc}$ region – the spatial mismatch (Section 1.1(2) (Part I)) expressed as a calibrated prediction rather than a degenerate one. Bishop and Swenson carry structurally equivalent Re^n entanglements, $0.0069\,\mathrm{Re}_b^{0.9}$ and $0.00459\,\mathrm{Re}_w^{0.923}$, paired with the correspondingly small prefactors that [2] identifies as their structural consequence. Bishop produces near-flat $T_w(x)$ profiles with a 5 K inlet-to-outlet variation and a faint local minimum at the $T_b \approx T_{pc}$ station: the $\mathrm{Nu}_{\mathrm{Bishop}}$ growth along the pipe (factor ∼2, Table 11) is compensated by the drop in λ_b through the pseudocritical region, and the heat transfer coefficient $\alpha = \mathrm{Nu}\,\lambda_b/d$

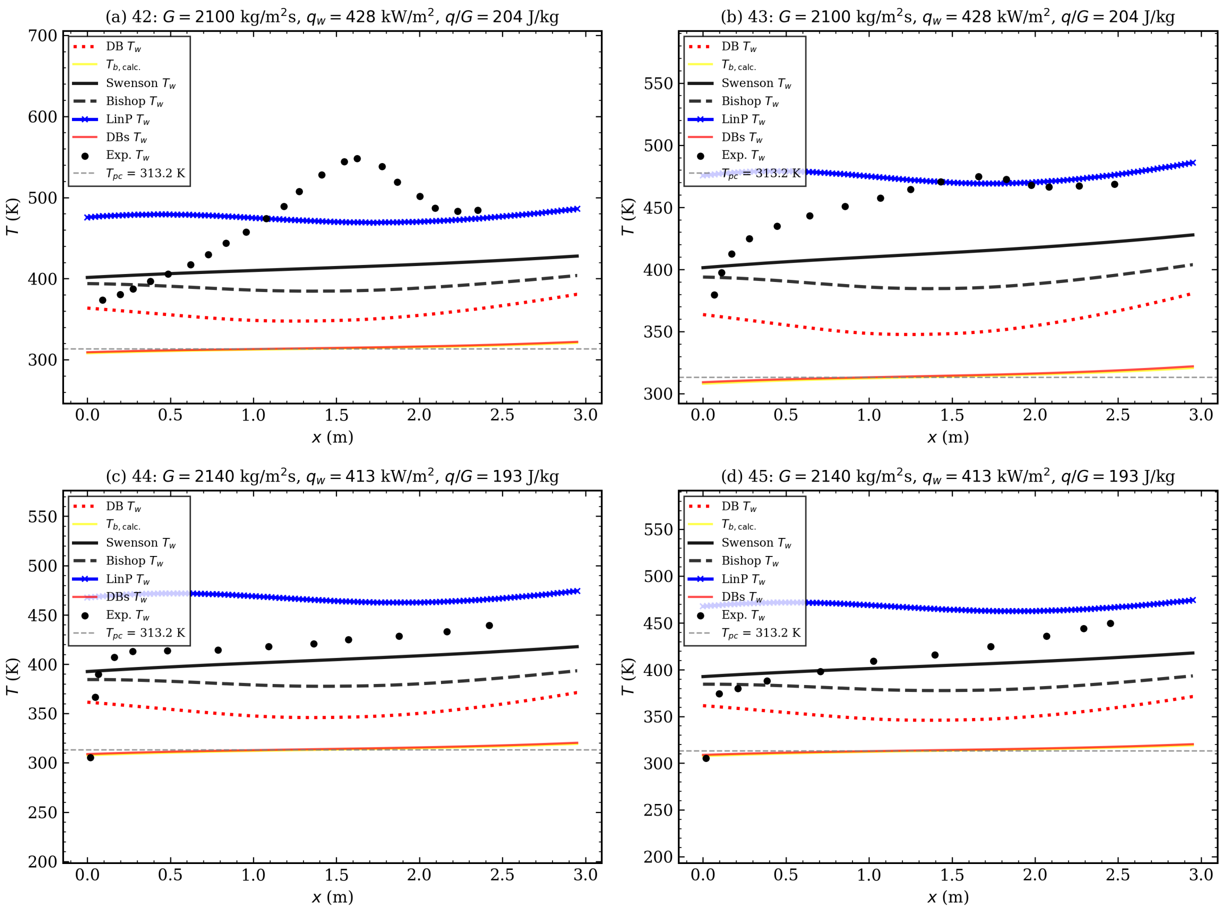

Figure 11: Predicted and experimental wall temperature profiles for the four JIHTRAS supercritical CO_2 cases (Table 4).

flattens into near-axial insensitivity. Swenson produces strictly linear $T_w(x)$ profiles with a $\sim 30\,\mathrm{K}$ rise between inlet and outlet: the wall-evaluated Reynolds and Prandtl numbers change little across the pipe because T_w is stably above T_{pc}, so $\mathrm{Nu}_{\mathrm{Swenson}}$ grows slowly and α evolves nearly linearly. Neither corrected correlation resolves the HTD structure; the mechanisms by which each one fails to do so are different – Bishop by growth–property cancellation, Swenson by wall-state stability – and both are direct extensions of the entanglement of [2] into the property-corrected correlation family.

LinP enters the JIHTRAS regime at the outer edge of its stated scope. The wall-to-bulk density ratio ρ_w/ρ_b is the largest in the database, and the pathway-resolved density correction that could resolve ρ_w/ρ_{pc} and ρ_{pc}/ρ_b within each pathway (Section 6 (Part I)) is absent from the linearised form. The consequence is visible directly in the axial profiles: LinP strongly overpredicts T_w for $x/L \lesssim 0.33$ in all four cases, matches the measured T_w on #42 for $x/L > 0.67$ and on #43 for $x/L > 0.47$, and approaches the data only near the outlet in #44 and #45. The failure to resolve the inlet HTD peak is not a feature the linearised pathway form was ever expected to capture; the conductance upper bound of Eq. (61) (Part I) limits how strongly the Prandtl-only correction can represent the barrier, and the variable-density contribution required to exceed this bound is the deferred refinement.

In the integrated metric, LinP nevertheless carries the best case RMS on #42 (59.1 K) and #43 (41.3 K), and the Swenson correlation shows better performance for #44 (30.3 K vs LinP's 71.0 K) and #45 (33.0 K vs LinP's 76.7 K). The ordering is consistent with the scope reading: where the wall-to-bulk contrast is slightly weaker and LinP recovers the outlet behaviour (#42, #43), LinP carries the lower RMS despite the inlet overprediction, because the residual is concentrated in the upstream third of the pipe; where the contrast is stronger and LinP approaches the data only at the outlet (#44, #45), Swenson's axial-flatness artefact happens to intersect the measured profile closely enough to carry the lower RMS, on the same mechanism exhibited in Kirillov #53 and #62. The JIHTRAS quartet thereby delimits the quantitative reach of the linearised pathway form and identifies the pathway-resolved $(\rho_w/\rho_b)^r$ correction as the missing ingredient, consistent with the bracket-function analysis of Figure 4 and the effective-weight drift of Figure 5.

The two worst case RMS values in the entire database are produced by the Swenson correlation on the NTUU downflow regimes: 317.6 K on #145 and 176.5 K on #104, against case-mean RMS values of 31.5 K for LinP, 47.9 K for Bishop, 54.3 K for Swenson, and 55.1 K for Dittus–Boelter across the eighteen-case database. The contrast across the four downflow cases – two NTUU with Swenson RMS 176–318 K, two JIHTRAS with Swenson RMS 33–43 K – establishes directly that the Swenson prediction is governed not by the physics of the heat transfer but by the geometric accident of where its near-linear $T_w(x)$ profile intersects the experimental measurement. On NTUU #104, where the bulk plateaus at T_{pc} across most of the pipe, the rigid Swenson profile sits 100 K above the experiment throughout and shows the second-largest RMS error in the database. On NTUU #145, where the bulk rises monotonically toward T_{pc} without crossing, the Swenson profile sits 300 K above the experiment and produces the largest RMS case in the database, recalling the strong-overprediction failure mode documented by [20] for wall-evaluated correlations in downflow regimes with a sustained near-T_{pc} bulk. On JIHTRAS #43, #45, where the bulk crosses T_{pc} linearly and the wall is stably above T_{pc}, the Swenson profile intersects the experimental $T_w(x)$ closely enough to carry the lowest case RMS on #45 – despite being the same wall-lock mechanism that fails catastrophically on the NTUU downflow cases, now expressed against a more favourable bulk trajectory. A correlation whose case RMS varies by nearly an order of magnitude across downflow regimes differing only in the axial shape of $T_b(x)$ is a correlation whose integrated metric tracks the experimental profile geometrically rather than physically. The scattered Swenson RMS wins across the database (Kirillov #53, #54, #62; Yamagata #111; JIHTRAS #44, #45) are therefore instances of a single structural artefact – a wall-evaluated correlation anchored on a thermodynamically stable wall state, producing a near-linear $T_w(x)$ that responds to the axial evolution of Re_w alone – appearing against six different bulk trajectories with six different integrated outcomes. Bishop fails comparably on these two regimes (RMS 43.6 K on #104, 175.1 K on #145), through its own one-sided entanglement failure: the bulk does not cross T_{pc} on #145, so the $\overline{\mathrm{Pr}}_b$ descent that drives Bishop's behaviour elsewhere in the database does not occur, and the correlation is left producing a nearly linear prediction well below the measurement.

The case-by-case reading of this subsection is the one that makes the pattern legible; the case-mean ordering LinP (31.5 K) < Bishop (47.9 K) < Swenson (54.3 K) < DB (55.1 K) quantifies it.

3.7 Structural summary of the validation

Eighteen cases across two fluids, three flow orientations, and reduced pressures from 1.065 to 1.22 test the three predictions of the scaling analysis against the experimental $T_w(x)$. The penetration scaling $\mathrm{Nu} \sim \sqrt{\mathrm{Re}}$ is confirmed by the largest within-pipe Reynolds lever arm in the database ($\mathrm{Re}_{b,\mathrm{out}}/\mathrm{Re}_{b,\mathrm{in}} \approx 2.3$–$3.0$ on the GK quartet) and by the opposite-sign Prandtl trajectory of the JIHTRAS CO_2 cases, which rules out a disguised Prandtl effect. The disentangled Prandtl correction $(\mathrm{Pr}_b/\mathrm{Pr}_w)^{1/4}$ is verified on the NTUU upflow quartet, in which Pr_b rises from 1.7 to 14 at nearly fixed Re_b and the entangled $\overline{\mathrm{Pr}}_b$ of Bishop and $\overline{\mathrm{Pr}}_w$ of Swenson drive step-like wall-temperature excursions of opposite sign that the bounded LinP factor does not carry. The analytical result of [2] that the DB prefactor 0.023 is the structural compensation for the $\mathrm{Re}^{0.8}$ overshoot is confirmed by the direct collapse of the uncalibrated DBs prediction onto the bulk-energy balance across all cases, and extends to Bishop and Swenson in modified form: the $\mathrm{Re}^{0.9}$ and $\mathrm{Re}^{0.923}$ entanglements of the two property-corrected forms produce axially flat $T_w(x)$ profiles in the high-Reynolds JIHTRAS regime by growth–property cancellation and wall-state stability respectively.

LinP carries the lowest case-mean Q-mode RMS across the eighteen cases (31.5 K, against 47.9 K for Bishop, 54.3 K for Swenson and 55.1 K for Dittus–Boelter), is the best model in nine of the eighteen cases, and achieves this with no fitted coefficient and no density-ratio correction. The case-by-case reading resolves the integrated ordering into its structural content: the one-sided entangled correlations reproduce the spatial-mismatch pathology of Section 1.1(2) (Part I) from opposite sides – Bishop bulk-locked through $\overline{\mathrm{Pr}}_b(T_b \to T_{pc})$, Swenson wall-locked through the thermodynamically stable wall state – and the accompanying $(\rho_w/\rho_b)^r$ factor attenuates but does not cure either pathology. The Yamagata quartet, which exchanges the wall and bulk roles between #111/#112 and #121/#122, completes the symmetry: the entanglement pathology is a property of whichever reference state passes through T_{pc}, not of the bulk state specifically. LinP, symmetric in wall and bulk by the $w = 1/2$ quadrature and using the bounded Prandtl-ratio correction, exhibits neither variant.

Two residual deficits localise LinP's quantitative reach. The JIHTRAS HTD peaks (#42–#45) lie in the strongest-contrast corner of the database, and the conductance upper bound of Eq. (61) (Part I) limits the Prandtl-only correction in this regime; the pathway-resolved ρ_w/ρ_b refinement that closes the gap is identified independently by the bracket-function departure above the parallel envelope in Figure 4 and the effective-weight drift of Figure 5, and is deferred to subsequent work. The NTUU and JIHTRAS downflow regimes lie at the edge of the forced-convection scope of the leading-order analysis: the matched upflow/downflow pairs #42/#43 and #44/#45 carry identical predicted $\mathrm{Nu}_b(x)$ by construction, while the measured $T_w(x)$ differs by an amount that reflects the buoyancy modification of the near-wall turbulence. The integrated metric conceals two further structural features of the case-by-case ordering: that the two worst case RMS values in the database (317.6 K and 176.5 K on NTUU downflow #145 and #104) are both produced by Swenson through the wall-lock mechanism identified in §3.6; and that the scattered Swenson RMS wins across the database are instances of a single structural artefact intersecting six different bulk trajectories with six different integrated outcomes. The case-mean ordering LinP < Bishop < Swenson < DB therefore quantifies a result that the case-by-case reading has already made structural: the symmetric two-point quadrature with $w = 1/2$ fixed by the unbiased-assignment argument and $\beta = 1/2$ fixed from an external-empirical prior outperforms three calibrated correlations carrying fitted coefficients, modified Prandtl numbers, and density-ratio corrections, across two fluids and three flow orientations, without recalibration.

4 Summary and open problems

4.1 Summary

The linearised pathway form derived in the companion paper [1],

$$\mathrm{Nu}_b = \sqrt{\mathrm{Re}_b}\,\mathrm{Pr}_b^{-1/2}\left(\frac{\mathrm{Pr}_b}{\mathrm{Pr}_w}\right)^{1/4}$$

with the symmetric pathway weight $w = 1/2$ and a priori fixed resistance exponent $\beta = 1/2$, was evaluated against an eighteen-case subset drawn from four experimental databases spanning supercritical water at 23.5–24.5 MPa and CO_2 at 9 MPa, with Reynolds numbers from 2.5×10^4 to 2×10^6, Prandtl numbers from 0.8 to 14, and upward, downward, and horizontal pipe geometries. Three correlations arranged along the entanglement axis served as comparators: [9] (bulk-anchored, entangled $\overline{\mathrm{Pr}}_b$, density ratio), [10] (wall-anchored, entangled $\overline{\mathrm{Pr}}_w$, density ratio), and Dittus–Boelter as the uncorrected baseline. Four results were established.

First, the diagnostic analysis of Section 2 confirmed, across 2201 experimental measurement stations, that the pathway formulation reduces the median impedance bias from 76 % (Dittus–Boelter) to 6 % (LinP), that the empirical bracket function $\mathcal{F}_{\mathrm{exp}}$ falls within the parallel-pathway envelope in the moderate-Prandtl-ratio regime and departs above it in the barrier-dominated regime $\xi \gtrsim 0.5$, and that the effective pathway weight $w_{\mathrm{eff}}(\theta_{pc})$ inverted from the experimental impedance crosses $w = 1/2$ at the bulk pseudocritical crossing across all fluids and Reynolds numbers, independently confirming the symmetric prior.

Second, penetration scaling $\mathrm{Nu} \sim \sqrt{\mathrm{Re}}$ is consistently preferred over $\mathrm{Re}^{0.8}$ whenever the pseudocritical barrier is active: the Grabezhnaya and Kirillov [5] cases ($\mathrm{Re}_{b,\mathrm{out}}/\mathrm{Re}_{b,\mathrm{in}} \approx 2.3$–$3.0$) provide the largest Reynolds-number lever arm within the pipe, and the JIHTRAS CO_2 cases, where Pr_b decreases along the pipe in contrast to the water datasets, rule out the alternative explanation that the fluid-specific Prandtl landscape, rather than the Reynolds exponent, drives the overprediction. A single uncalibrated prefactor $C = 1$ works for both fluids. The disentangled Prandtl correction $(\mathrm{Pr}_b/\mathrm{Pr}_w)^{1/4}$, verified with the NTUU upflow quartet in which Pr_b rises from 1.7 to 14 at nearly fixed Re_b, avoids the $\overline{\mathrm{Pr}}$ divergence that drives both [9] and [10] into step-like T_w excursions of opposite sign. The analytical result of [2] – that the Dittus–Boelter prefactor 0.023 is the structural compensation for the $\mathrm{Re}^{0.8}$ overshoot – is confirmed directly by the collapse of the uncalibrated DBs prediction onto the bulk-energy balance across all cases, and extends to the modified form of [9] and [10] through their $\mathrm{Re}^{0.9}$ and $\mathrm{Re}^{0.923}$ entanglements.

Third, the Yamagata et al. [6] quartet, which exchanges the wall and bulk roles between #111/#112 (wall crosses T_{pc}) and #121/#122 (bulk crosses T_{pc}), establishes that the spatial-mismatch pathology is a property of whichever reference state traverses the pseudocritical temperature, not of the bulk state specifically. The pairs #111/#112 and #121/#122 are the bottom- and top-wall records of the same two horizontal runs, so the role swap is realised within identical hydraulic conditions. Each one-sided entangled correlation reproduces the pathology when its own reference state crosses, and the accompanying factor $(\rho_w/\rho_b)^r$ attenuates but does not cure either variant. LinP, symmetric in wall and bulk by the $w = 1/2$ quadrature and using the bounded Prandtl-ratio correction, exhibits neither variant. The scattered RMS wins of [10] across the database are instances of a single structural artefact – a wall-evaluated correlation anchored on a thermodynamically stable wall state, producing a near-linear $T_w(x)$ that responds to the axial evolution of Re_w alone – whose integrated error varies by nearly an order of magnitude across downflow regimes differing only in the axial shape of $T_b(x)$, demonstrating that the correlation's case-mean metric tracks the experimental profile geometrically rather than physically.

Fourth, uncalibrated LinP carries the lowest case-mean Q-mode wall-temperature root-mean-square error across the eighteen cases: 31.5 K, against 47.9 K for [9], 54.3 K for [10], and 55.1 K for Dittus–Boelter. LinP is the best model in nine of the eighteen cases, with no fitted coefficient and no density-ratio correction.

The quantitative reach of the linearised form is delimited by two residual deficits, both identified independently by the impedance diagnostics of §2. In the JIHTRAS heat-transfer-deterioration regime the wall-to-bulk density contrast drives LinP against its parallel-pathway upper bound, consistent with the bracket-function departure above the parallel envelope and the effective-weight drift for $\theta_{pc} > 1/2$. In the NTUU and JIHTRAS downflow regimes buoyancy modifies the near-wall turbulence and leaves the forced-convection scope of the leading-order analysis. Both deficits point to the same missing ingredient: the pathway-resolved ρ_w/ρ_b-correction that resolves the density contrast within each pathway, which lies beyond the linearised form.

4.2 Open problems

Two open problems are identified by the validation, ordered by increasing difficulty.

(i) The pathway-resolved density-ratio correction. The bracket-function analysis of Figure 4(b) locates the departure of the experimental $\mathcal{F}_{\mathrm{exp}}$ above the parallel envelope in the barrier-dominated regime $\xi \gtrsim 0.5$, where $\mathrm{Pr}_b/\mathrm{Pr}_w$ is large enough that the pseudocritical property peak impedes turbulent transport across the boundary layer. The effective pathway weight $w_{\mathrm{eff}}(\theta_{pc})$ of Figure 5 crosses 1/2 at the bulk crossing $\theta_{pc} \approx 0$ – independently of fluid, Reynolds number, and pressure – and drifts upward for $\theta_{pc} > 1/2$ in a manner organised by the barrier position. The two diagnostics converge on the same refinement: a pathway-resolved density correction that resolves ρ_w/ρ_{pc} and ρ_{pc}/ρ_b within each pathway, equivalent to a θ_{pc}-structured weight $w(\theta_{pc})$ anchored at $w(0) = 1/2$, whose construction is left to subsequent work. The diagnostic machinery of Section 2 provides the tools to constrain this refinement empirically.

(ii) Buoyancy within the pathway framework. The four downflow cases in the present database (NTUU #104, #145, and the JIHTRAS pairs #43, #45) all satisfy the nominal forced-convection criterion $\mathrm{Ri} = \mathrm{Gr}/\mathrm{Re}_b^2 < 0.105$, yet the measured $T_w(x)$ on the matched JIHTRAS upflow/downflow pairs #42/#43 and #44/#45, identical bulk thermodynamics by construction, differs by amounts that the forced-convection analysis cannot recover. The near-pseudocritical sensitivity of the buoyancy modification of the near-wall turbulence below the conventional Ri threshold is documented in the supercritical literature [20] and constitutes a scope extension rather than a correction within the present framework. Incorporating the buoyancy flux into the pathway weight, or into a second-order density refinement, would extend the scope of the linearised form to mixed-convection regimes; the diagnostic analysis provides the tools to constrain the extension empirically.

References

[1] I. Otić, O. Ertunç, The thermal impedance integral and the pathway decomposition of supercritical turbulent heat transfer. Part I. Framework, KITopen, preprint (2026). doi:10.5445/IR/1000196040.

[2] I. Otić, O. Ertunç, The Reynolds-number scaling of the Lyon integral and the structural rigidity of the Dittus–Boelter correlation, Preprint, KITopen, 2026.

[3] V. G. Razumovskiy, E. N. Pis'mennyi, K. Sidawi, I. L. Pioro, A. E. Koloskov, Experimental heat transfer in an annular channel and 3-rod bundle cooled with upward flow of supercritical water, Journal of Nuclear Engineering and Radiation Science 2 (2016) 011010. URL: https://doi.org/10.1115/1.4031818. doi:10.1115/1.4031818.

[4] International Atomic Energy Agency Technical Document, Understanding and prediction of thermohydraulic phenomena relevant to supercritical water cooled reactors (SCWRs), Technical Report IAEA-TECDOC-1900, International Atomic Energy Agency, Vienna, 2020. URL: https://www.iaea.org/publications/13636/understanding-and-prediction-of-thermohydraulic-phenomena-relevant-to-supercritical-water-c

[5] V. Grabezhnaya, P. Kirillov, Heat transfer under supercritical pressures and heat transfer deterioration boundaries, Thermal Engineering 53 (2006) 296–301. doi:10.1134/S0040601506040069.

[6] K. Yamagata, K. Nishikawa, S. Hasegawa, T. Fujii, S. Yoshida, Forced convective heat transfer to supercritical water flowing in tubes, International Journal of Heat and Mass Transfer 15 (1972) 2575–2593. doi:10.1016/0017-9310(72)90148-2.

[7] V. Kurganov, A. Kaptil'ny, Velocity and enthalpy fields and eddy diffusivities in a heated supercritical fluid flow, Experimental Thermal and Fluid Science 5 (1992) 465–478. URL: https://www.sciencedirect.com/science/article/pii/0894177792900332. doi:https://doi.org/10.1016/0894-1777(92)90033-2.

[8] V. A. Kurganov, A. G. Kaptil'nyi, Flow structure and turbulent transport of a supercritical pressure fluid in a vertical heated tube under the conditions of mixed convection. experimental data, International Journal of Heat and Mass Transfer 36 (1993) 3383–3392. doi:10.1016/0017-9310(93)90020-7.

[9] A. Bishop, R. Sandberg, L. Tong, Forced convection heat transfer to water at near-critical temperature and supercritical pressures, Technical Report WCAP-2056, Westinghouse Electric Corporation, Pittsburg, USA, 1964. (see also AICE, J. Chemical Engineering Symposium Series, No 2. London: Institute of Chemical Engineers, 1965).

[10] H. Swenson, J. Carver, C. Kakarala, Heat transfer to supercritical water in smooth-bore tubes, Trans. ASME, J. Heat Transfer, C 87 (1965) 477–484. doi:10.1115/1.3689139.

[11] Y. A. Çengel, A. J. Ghajar, Heat and Mass Transfer: Fundamentals and Applications, 5th ed., McGraw-Hill Education, New York, 2015.

[12] J. Jackson, Fluid flow and convective heat transfer to fluids at supercritical pressure, Nuclear Engineering and Design 264 (2013) 24–40. URL: https://www.sciencedirect.com/science/article/pii/S0029549313000976. doi:https://doi.org/10.1016/j.nucengdes.2012.09.040, sI:NURETH-14.

[13] I. H. Bell, J. Wronski, S. Quoilin, V. Lemort, Pure and pseudo-pure fluid thermophysical property evaluation and the open-source thermophysical property library CoolProp, Industrial & Engineering Chemistry Research 53 (2014) 2498–2508. URL: https://doi.org/10.1021/ie4033999. doi:10.1021/ie4033999, the project website: http://www.coolprop.org.

[14] S. E. Haaland, Simple and explicit formulas for the friction factor in turbulent pipe flow, Journal of Fluids Engineering 105 (1983) 89–90. doi:10.1115/1.3240948.

[15] F. W. Dittus, L. M. K. Boelter, Heat Transfer in Automobile Radiators of the Tubular Type, Technical Report 13, University of California, Berkeley, Calif., 1930. Reprinted in International Communications in Heat and Mass Transfer, Vol. 12, pp. 3–22, 1985.

[16] X. Zhao, W. Ambrosini, A. Pucciarelli, S. Kassem, T. Varju, A. Kiss, I. Otić, Y. Filonova, V. Filonov, Y. Zhu, B. Bi, Report on the results of the benchmark exercise, Technical Report Deliverable D3.2, ECC-SMART, 2023. URL: https://cordis.europa.eu/project/id/945234/.

[17] W. Ambrosini, I. Otić, T. Schulenberg, A. Pucciarelli, O. Chaaraoui, T. Varju, A. Kiss, B. Babcsány, C. Antók, P. Mészáros, Z. Bertesina, S. Czifrus, V. Filonov, D. Fedorov, Y. Filonova, Y. Dubyk, A. Nava-Dominguez, X. Zhao, Report on the preconceptual studies on the core layout and passive safety concept of the SCW-SMR, Technical Report Deliverable D3.3, ECC-SMART, 2024.

[18] T. Varju, A. Csige, A. Kiss, V. Filonov, Y. Filonova, D. Fedorov, A. Pucciarelli, S. Kassem, W. Ambrosini, Discussion and perspectives for improvements of heat transfer correlation capabilities for fluids at supercritical pressures, Nuclear Engineering and Design 421 (2024) 113085. URL: https://doi.org/10.1016/j.nucengdes.2024.113085. doi:10.1016/j.nucengdes.2024.113085.

[19] S. Mokry, I. Pioro, A. Farah, K. King, S. Gupta, W. Peiman, P. Kirillov, Development of supercritical water heat-transfer correlation for vertical bare tubes, Nuclear Engineering and Design 241 (2011) 1126–1136. URL: https://www.sciencedirect.com/science/article/pii/S0029549310004310. doi:https://doi.org/10.1016/j.nucengdes.2010.06.012, international Conference on Nuclear Energy for New Europe 2009.

[20] V. Kurganov, Y. Zeigarnik, I. Maslakova, Heat transfer and hydraulic resistance of supercritical pressure coolants. part iii: Generalized description of scp fluids normal heat transfer, empirical calculating correlations, integral method of theoretical calculations, International Journal of Heat and Mass Transfer 67 (2013) 535–547. doi:10.1016/j.ijheatmasstransfer.2013.07.056.